CHALMERS
UNIVERSITY OF TECHNOLOGY

Development of SAFER HBM v11

Report 2024:06, Version 1.0

Main Author

Johan Iraeus

Co-authors and Reviewer(s) of the report

Erik Brynskog, Jobin John, Jonas Östh, Bengt Pipkorn, Johan Davidsson

Funding

This study was funded by Strategic Vehicle Research and Innovation (FFI) (Award number: 2022-01654), by VINNOVA, the Swedish Transport Administration, Swedish Energy Agency, and industrial partners. Partners in the research project are Autoliv, Volvo Cars and Sahlgrenska University Hospital, Gothenburg, Sweden. This work has been carried out in association with SAFER – Vehicle and Traffic Safety Centre at Chalmers, Gothenburg, Sweden. The simulations were enabled by resources provided by the National Academic Infrastructure for Supercomputing in Sweden (NAISS) at Chalmers Centre for Computational Science and Engineering (C3SE) and at Linköping University National Supercomputer Centre (NSC).

DEPARTMENT OF MECHANICS AND MARITIME SCIENCES
CHALMERS UNIVERSITY OF TECHNOLOGY

REPORT 2024:06
Gothenburg, Sweden, Dec 2024
www.chalmers.se

Contents

1. Introduction

The development of SAFER HBM started in 2008, when the first human body modelling (HBM) project was initiated by members of the SAFER - Vehicle and Traffic Safety Centre. Although the project contributors have varied over the years, the core SAFER HBM contributors are Autoliv, Chalmers and Volvo Cars. The objective from the start was, and still is, to develop an "omnidirectional, tunable and scalable HBM capable of injury risk and biofidelic kinematics prediction in high-g as well as low-g events". Up until 2017, the model was called SAFER THUMS, as up until that point the THUMS version 3 model was used, with add-on active muscles (Östh et al., 2012), and retuned material parameters of the chest (Mendoza-Vazquez et al., 2013). As these modifications were carried out by different researchers in different projects, two versions were available, one version with muscle and muscle control system implemented, referred to as active SAFER THUMS for prediction of low-G kinematics, and a passive SAFER THUMS for kinematic predictions and injury evaluation in high-G loading.

However, by the release of version eight in 2017, see Figure 1 (left), the model got rebranded to SAFER HBM, to acknowledge the contributors association to SAFER. For this version, the base model was the passive SAFER THUMS including two major updates; the head model which was changed to the Royal Institute of Technology FE head model (KTH model) (Kleiven, 2007), and the ribcage model, which was changed to a new generic ribcage based on a statistical shape model representing a population average (Iraeus et al., 2020; Iraeus & Pipkorn, 2019).

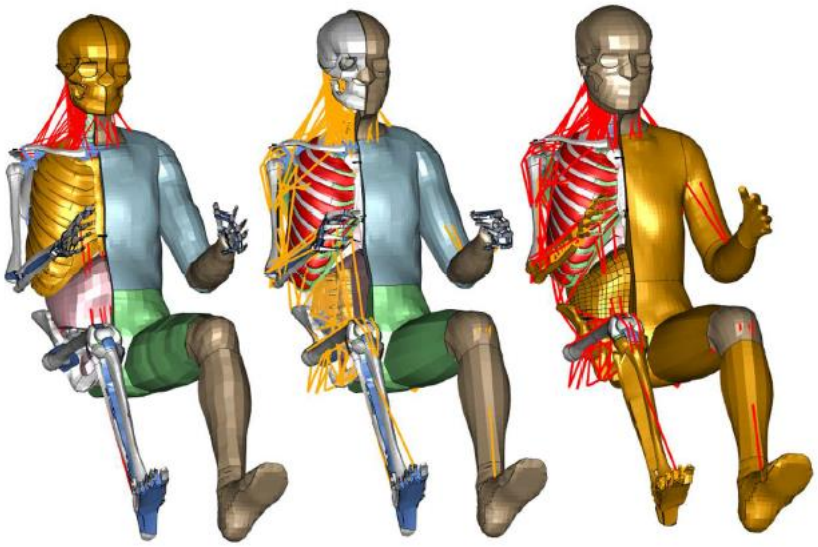

Figure 1. Left to right; Version eight (2017), version nine (2018) and version 10 (2020) of the SAFER HBM. Updated body parts for each model are colored gold. Figure from (Pipkorn et al., 2023).

With the release of version nine in 2018, the active muscles with postural feedback controllers (Ólafsdóttir et al., 2019; Östh et al., 2015; Östh et al., 2012), from the active SAFER THUMS, were integrated into the SAFER HBM version eight, to form one base model, see Figure 1 (middle). Parameters were introduced to turn on/off active muscles

and to define controller reference times, with the overall purpose of being able to run pre-crash and in-crash seamlessly. The lumbar and neck muscle controllers were further developed using spatial tuning patterns to enable biofidelic response to omni-directional loading (Larsson et al., 2019). As the active and passive models were merged, some soft tissue passive material properties that originally were too stiff in low-G loading, needed to be updated (Larsson, 2020).

In 2020, SAFER HBM was updated to version 10, see Figure 1 (right). In this update the pelvis was changed to a new FE-model based on the average shape of a male occupant from a statistical shape model (Brynskog et al., 2021). The KTH head and brain model was updated with a brain stem. In addition, updates to the lower arms, lower legs, and torso subcutaneous soft tissues were introduced to refine the mesh and create a continuous mesh over the shoulder and hip joints. The geometry for these updates were based on a statistical shape model predicting an average male outer shape (Reed & Ebert, 2013). Finally, the skeletal bones of the lower arm (Bayat & Pongpairote, 2020), and the lower leg (Roberts, 2020) were updated. The new lower arm was meshed to fit the SAFER HBM geometry, while the lower leg was originally developed to represent an average female and was scaled to fit the SAFER HBM average male anthropometry.

The SAFER HBM base model represents a 45-year-old average sized male (1750 mm and 77kg) according to the definitions in (Schneider, 1983).

The model validation and associated injury risk functions for SAFER HBM have continuously been reported in open literature. Some of the early validation work is now obsolete, as new body parts have been introduced, and no references to these will be made here. The head and brain model are validated for intracranial pressure as well as for frontal, occipital and lateral impacts (Kleiven, 2006; Kleiven & Hardy, 2002; Kleiven & Von Holst, 2002a, 2002b) and have an injury risk function based on NFL head impact reconstructions (Fahlstedt et al., 2022; Kleiven, 2007). The ribcage has been validated for kinetics, kinematics and rib strain (Iraeus & Pipkorn, 2019) with the strain-based injury risk function validated on multiple scales, from isolated ribs to whole body subjected to belt loads in a sled setup (Pipkorn et al., 2019). The most recent rib fracture injury risk function with re-validation of SAFER HBM is found in (Larsson et al., 2021). The validation of the lower arm including risk estimation is found in (Bayat & Pongpairote, 2020).

The latest version of SAFER HBM, version 11 presented in this report, was developed to be a stand-alone model, free from proprietary data from the original THUMS model, with special focus on injury prediction for reclined occupants in front crashes.

The objective of this report is to describe the SAFER HBM updates from version 10 to version 11, and the additional validation that has been carried out, and is summarized, in a validation repository.

2. Model updates

From version 10 to version 11 several updates have been introduced. Some updates were introduced to replace third party proprietary information (from the original THUMS model), while others were to improve the biofidelity. Specifically, the following updates were included:

- Updates to the pelvis to improve the overall biofidelity and specifically to improve prediction of submarining.
- Updates to the femur to prepare the model for tissue-based injury risk assessment in these bones.
- Updates to the lumbar spine to improve overall biofidelity, and to enable prediction of compression fracture in the lumbar spine vertebrae bodies.
- Update to the thoracic and cervical spine to make the spine modelling consistent for the whole spine (based on the modelling of the lumbar spine), improve the overall biofidelity, and prepare the model for future updates, including fracture prediction also for the thoracic and cervical spine.
- Updates to the clavicula, scapula and humerus to prepare the model for tissue-based injury risk assessment in these bones.
- Updates to the costovertebral joints to connect the updated spine to the ribs.
- Updates to the soft tissues to improve overall biofidelity and numerical robustness, remove proprietary information, and specifically to improve the prediction of submarining.
- Update of the discrete muscle elements (mainly for the back) to improve biofidelity and to facilitate that flexors and extensors have the correct function even when the spine curvature changes.
- Finally, the whole model was renumbered, and fitted into a smaller number range, to enable the use of several SAFER HBMs in one vehicle model, while keeping the total HBM numbering within 10M range.

Each of these updates will be described in detail in the sections below.

Generally, where the mesh was updated, the minimum element size was based on a target time step of 0.5 µs in explicit FE solvers. Also, generally, reduced integration solid elements (LS-DYNA type 1) are used for modelling trabecular bones, full integration shell elements (LS-DYNA type 16) for modelling cortical bones, and full integration solid elements (LS-DYNA type -2) are used to model soft tissue. Deviations from this will be presented below. All elements of the model conform with the 100% quality criteria defined in Appendix A.

2.1. Updates to the Pelvis

The pelvis was updated to improve overall biofidelity, allow for population-based variations in pelvis shape through morphing, prepare it for future fracture predictions with strain-based injury risk functions (IRFs), and to improve submarining prediction. The updates have been described in detail in (Brynskog et al., 2022, 2024a). In summary, a new mesh was built based on the average pelvis shape of 132 subjects (75 females and 57 males) (Brynskog et al., 2021), see Figure 2. The cortical bone was modelled using quadrilateral shell elements on the surface of the trabecular bone,

which was modelled using hexahedral solid elements generated by ANSA (Beta CAE Systems, Switzerland) hexa blocks. The thickness of the innominate bone cortical shells was taken from the average subject found from 10 controls (5 male, 5 female) and had a thickness range of 0.5 – 5.0 mm (Harris et al., 2012). The sacrum cortical thickness was set at a constant value of 1.3 mm for the entire sacrum (Peretz et al., 1998; Richards et al., 2010), since more detailed data was not available. For the elastic-plastic isotropic material properties of the cortical bone, Young's modulus 10.96 GPa and yield stress 57.5 MPa were used, based on (Kemper et al., 2008), while the elastic-perfect plastic isotropic material properties for the trabecular bone used Young's modulus 0.07 GPa and yield stress 0.57MPa, based on (Dalstra & Huiskes, 1995).

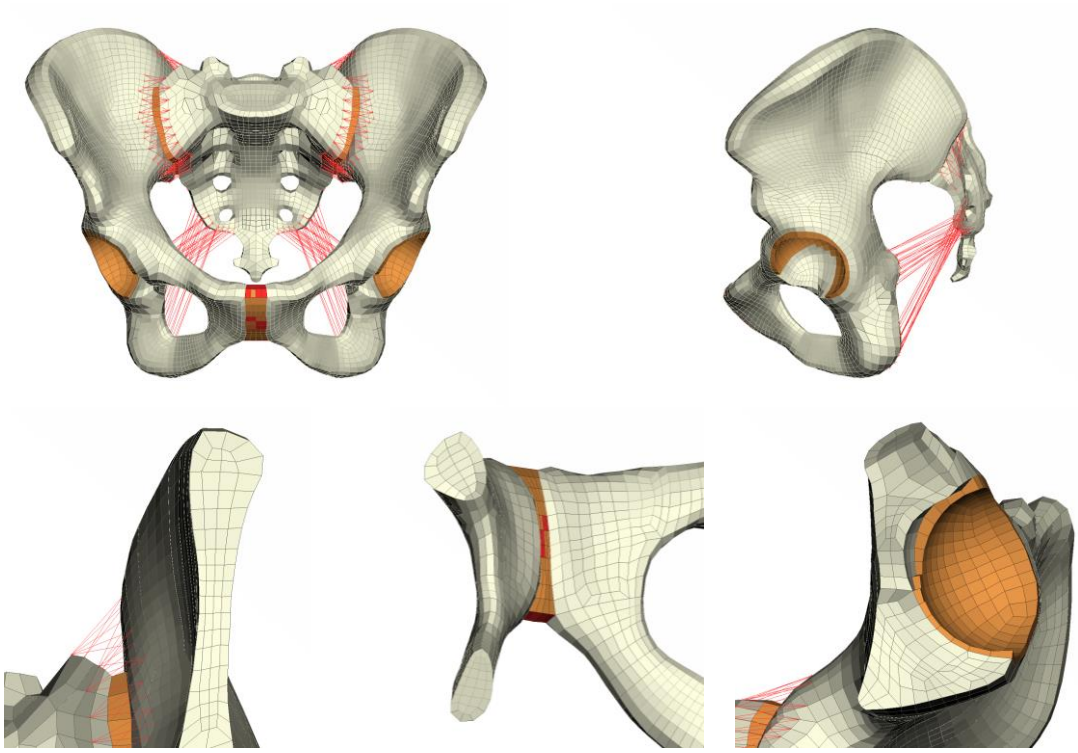

Figure 2. The new pelvis model of the average pelvis shape. The top row shows a front and lateral view of the model while the bottom row shows the FE-mesh at key cross-sections (iliac wing (left), pubic bones (middle), acetabulum (right)).

The pubis symphysis (PS) joint was modelled as a solid disc, using fully integrated (LS-DYNA type 2) hexahedral elements, with ligaments covering its surface, using fully integrated (LS-DYNA type 16) quadrilateral elements, Figure 3. The thickness of the ligaments was uniformly set to 1 mm while the average thickness at its anterior, middle, and posterior side was defined to match reported averages (Alicioglu et al., 2008). Lacking well-defined material data for the disc and ligaments individually, the joint was modelled using a rubber material model with stress-strain response calibrated against component tests by (Dakin et al., 2001), to match the average tension/compression response. For the response after tuning see Section 3.1.

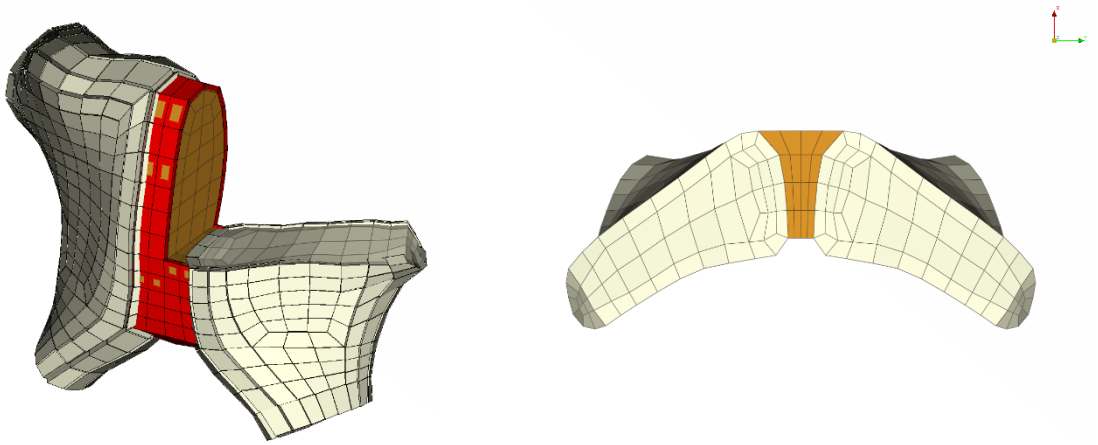

Figure 3. Pubis symphysis joint FE-model.

The sacroiliac (SI) joint was modelled as a synovial region, representing cartilage, and the anterior, posterior, and interosseous SI ligaments, Figure 4. The synovial region was modeled with fully integrated solid elements (LS-DYNA type 2) with a surface area based on (Casaroli et al., 2020), and a thickness ranging from 2.5-4.5 mm. On the sacral side, the elements were connected by sharing nodes with the cortical surface, while a friction contact was defined towards the innominate bone. Lacking material data, the same cartilage material as was calibrated for the PS disc was used also for the synovial elements. Dimensions for the ligaments were based on average origin area in (Steinke et al., 2010), Table 1, with the anterior and posterior ligaments represented by crossing cable elements while the interosseous ligament was modelled as fully integrated solid elements (LS-DYNA type -2). In addition, the sacrotuberous and the sacrospinous ligaments, spanning from the innominate bone to the sacrum, were modelled by straight cable elements with approximate dimensions from (Hammer et al., 2009), Figure 5 and Table 1. Lacking alternative material data, the ligaments were modelled based on the calibrated material properties presented by (Ivanov et al., 2009), and the complete SI stiffness response was evaluated against component tests by (Miller et al., 1987), see Section 3.1.

Table 1. Ligament dimensions.

Ligament	Average area	Reference	No. elements in model	Area in FE-model
ASL	130 mm^2	(Steinke et al., 2010)	60 (per side)	2.17 mm^2/cable
PSL	151 mm^2	Steinke et al., 2010)	57 (per side)	2.65 mm^2/cable
ISL	724.5 mm^2	Steinke et al., 2010)	Solids	760 mm^2 total
STL	42.2 mm^2	(Hammer et al., 2009)	18 (per side)	2.34 mm^2/cable
SSL	30.6 mm^2	(Hammer et al., 2009)	24 (per side)	1.275 mm^2/cable

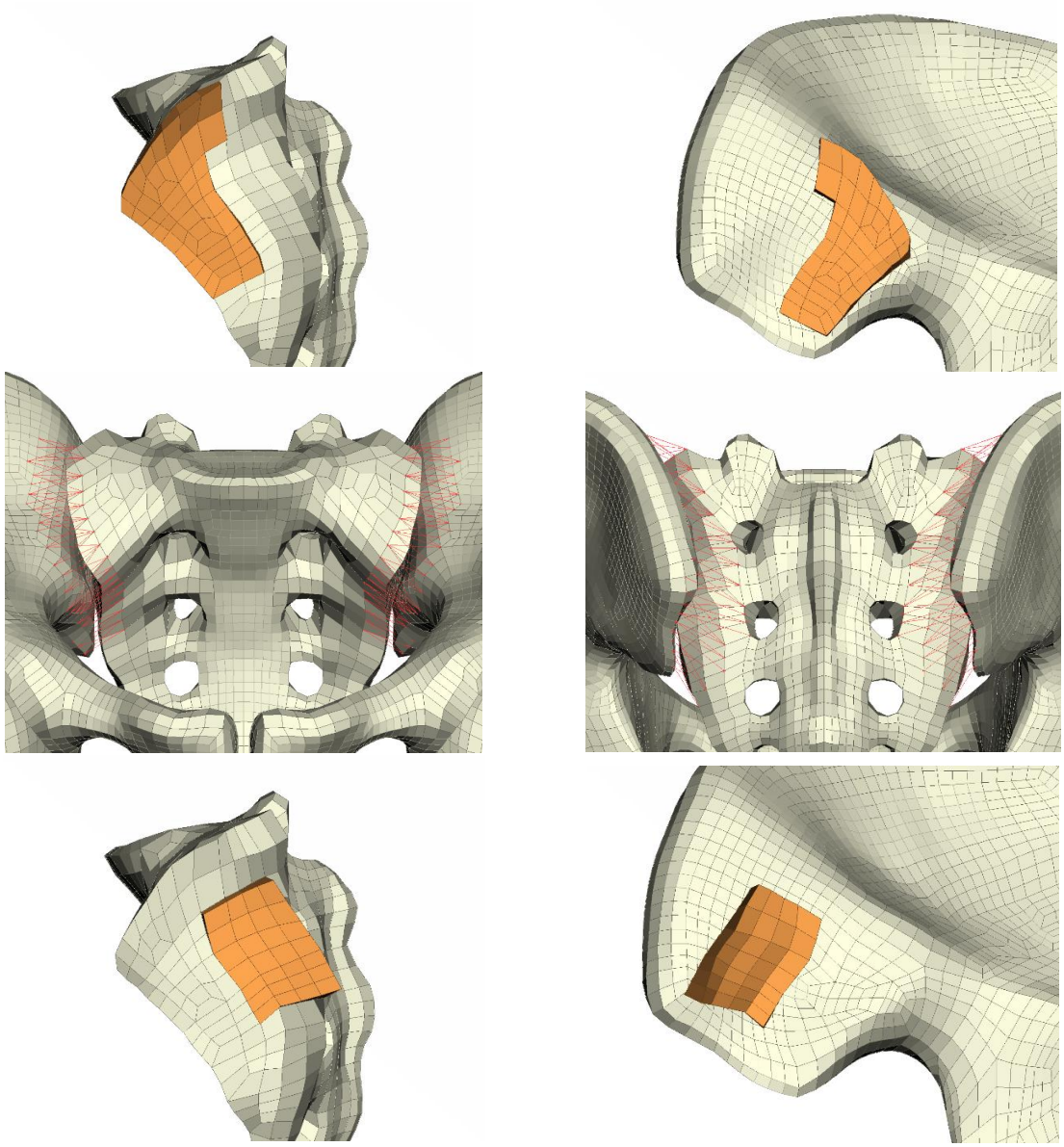

Figure 4. Sacroiliac joint FE-model. Synovial region (top), anterior ligaments (middle, left), posterior ligaments (middle, right), and interosseous ligaments (bottom).

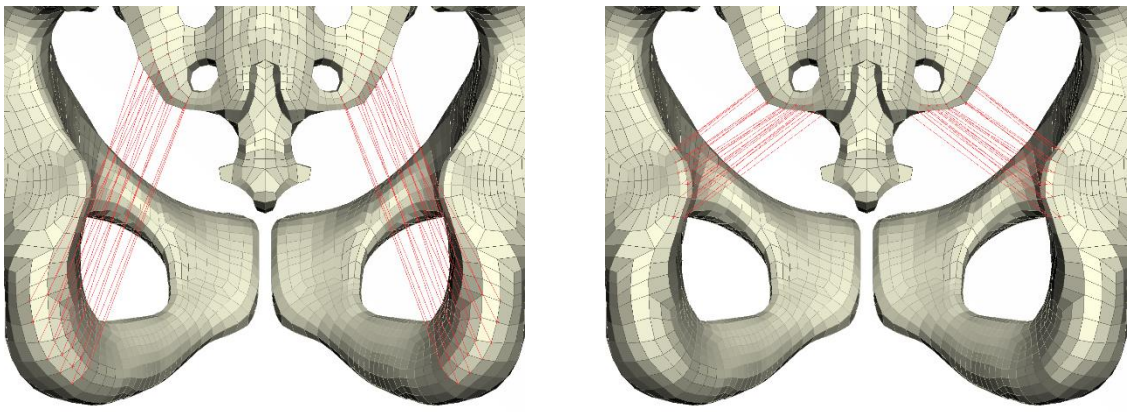

Figure 5. Sacrotuberous ligaments (left) and sacrospinous ligaments (right).

The pelvis FE-model is linked with a statistical shape model (Brynskog et al., 2021), allowing for mesh morphing to a population of vehicle occupants, see (Brynskog et al., 2022). For SAFER HBM, the pelvis of an average male (age = 45 years, stature = 1750 mm, weight = 77 kg) was predicted, see Figure 6. Since the shape model is built on complete pelvises, the predicted shape is not perfectly symmetric. To have a symmetric baseline, the average of the left/right prediction was computed and mirrored before aligning the mid-plane with the sagittal plane at Y=0. When integrating the pelvis into the full-body SAFER HBM, the pelvis was positioned to have a pelvis angle of 45°, matching the reported average from (Izumiyama et al., 2018).

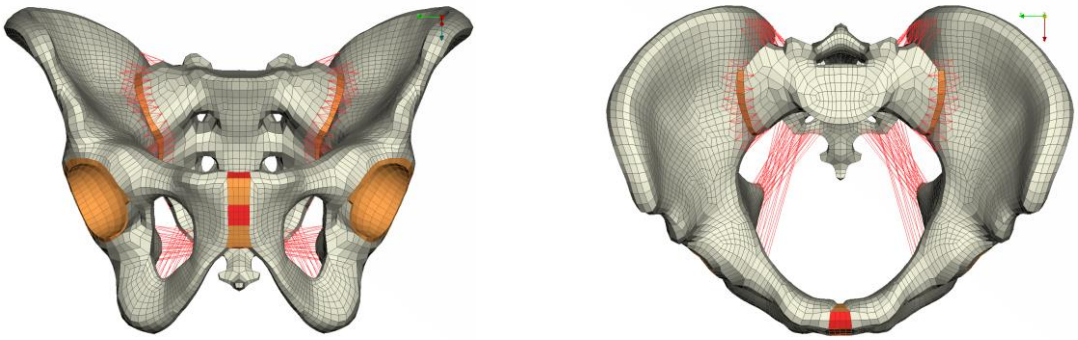

Figure 6. The FE-model morphed to an average male (45 years, 175 cm, 77 kg using the statistical shape model prediction.

2.2. Updates to the Femur

The femur model was updated to enable tissue-based injury criteria in the future and has previously been presented in (Svensson, 2022). The geometry was based on a scaled geometry (+10% in all directions, to fit to the SAFER HBM dimensions) of an average sized female (Gayzik et al., 2011). An all-hexahedral mesh was created using the ANSA hexa block strategy. The element size for the new mesh was biased towards the smallest size, without getting excessive mass scaling for the targeted HBM time step. The cortical bone of the femur was modelled using solid elements. Two elements through the thickness at the shaft, and one element over the thickness at the distal and proximal ends, see Figure 7.

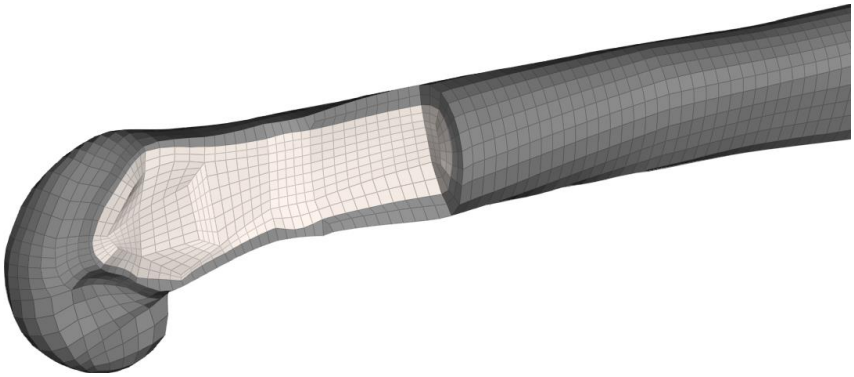

Figure 7. The updated mesh of the femur. The gray elements represent the cortical bone and the beige elements the trabecular bone.

The thickness of the cortical bone in the shaft was based on (Someya et al., 2020), with the proximal end based on (Malo et al., 2013) and the distal end based on (Du et al., 2018). The resulting thickness distribution is presented in Figure 8. The material properties of the cortical bone were modelled according to data from (Bayraktar et al., 2004), using an isotropic elastic-perfect plastic material model with Young's modulus 19.9 GPa and yield stress 108 MPa. The material property of the trabecular bone was modelled using an isotropic linear elastic material model with Young's modulus of 0.2 GPa, according to (Martin et al., 1998).

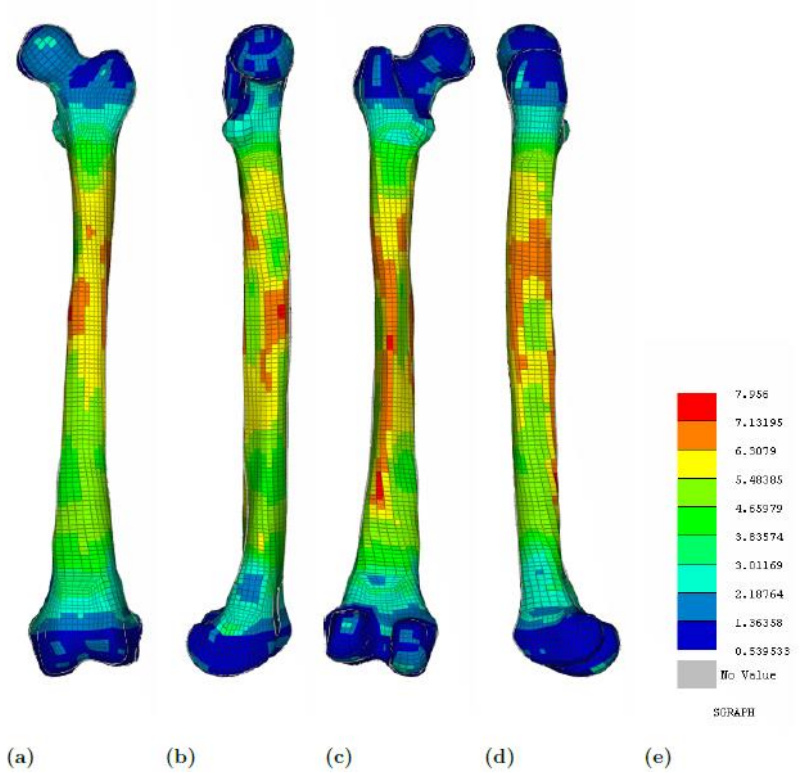

Figure 8. The thickness distribution of the femur model displayed from; (a) anterior, (b) medial, (c) posterior, and (d) lateral sides. The fringe is displayed in millimeters (with a maximum thickness of 8 mm and a minimum thickness of about 0.5 mm. From (Svensson, 2022).

The femur model dimensions were verified to measurements of 62 male subjects (Klein et al., 2015). The average overall length in the Klein et al. study was 481mm, compared to the 473mm length of the femur model. In Figure 9 the model cross-section (total and cortical bone) is compared to data from the same study, showing that the model is within the subject variability (and close to the average), except for the cortical cross-sectional area at measurement location 5 (which is located 25% from the distal end).

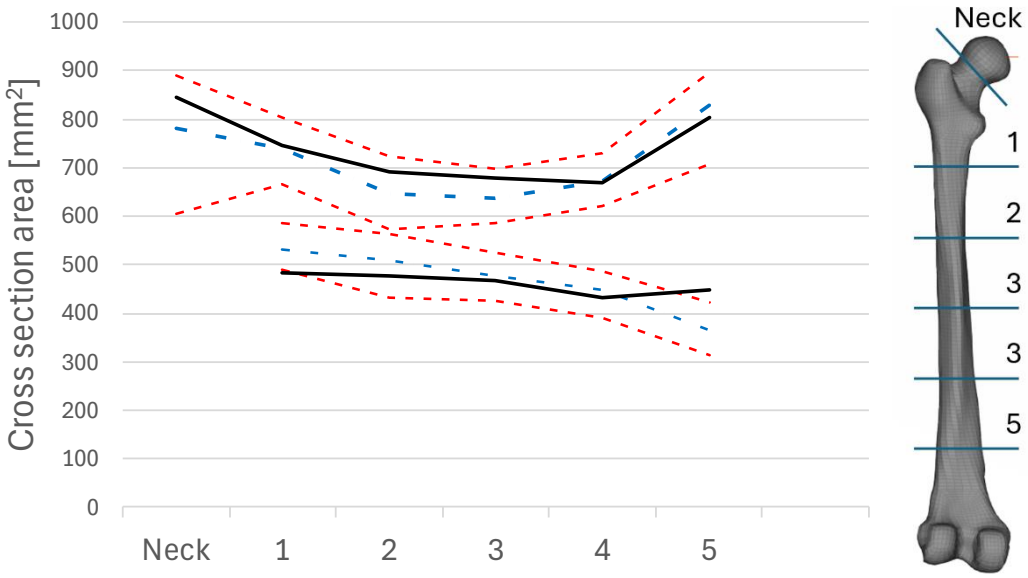

Figure 9. Verification of femur cross sectional area. The upper results correspond to the total cross-sectional area, while the lower corresponds to the cortical bone cross sectional area. Blue curves are the average values from (Klein et al., 2015), while red are the min/max values. The black curves represent the cross-sectional properties for the model.

2.3. Updates to the Lumbar Spine

The lumbar spine was updated with the aim of predicting compression fractures, using a tissue-based fracture criterion. The updates to the lumbar spine have been described in detail in (Iraeus et al., 2023). In summary, a new mesh was created based on a geometry of an average sized female (Gayzik et al., 2011). An exemplary mesh of the L4-L5 mesh can be seen in Figure 10. The mesh pattern was laid out to give nodal connectivity between the vertebrae bodies and the discs. The vertebrae cortical bone was modelled using quadrilateral shell elements, and the trabecular bone using hexahedral solid elements, using ANSA hexa blocks. The thicknesses of the cortical shells were based on (Edwards et al., 2001), and ranges between 0.51 and 0.82 mm. The orthotropic material parameters for the cortical bone were based on (Khor et al., 2018), while the anisotropic material parameters (with the inferior-superior being the main material direction) for the trabecular bone were based on (Kopperdahl et al., 2002; Ulrich et al., 1999).

The disc nucleus and annulus ground substance were modelled using solid elements (LS-DYNA type 1 with HG formulation 5), while the annulus fiber layers each are modelled using two layers of shell elements (with coincident nodes and with fiber angles in plus/minus directions). The material properties of the annulus ground substance were based on (Panzer & Cronin, 2009). The fiber angles and membrane thicknesses, which vary through the thickness of the annulus, were based on (Alonso & Hart, 2014; Cassidy et al., 1989). The material properties for the fibers were based on (Cassidy et al., 1989; Holzapfel et al., 2005). The ligaments, seen as red lines in Figure 10, were modelled using beam elements, with physical properties defined using force-elongation properties from (Chazal et al., 1985; Mattucci & Cronin, 2015; Nolte et al., 1990).

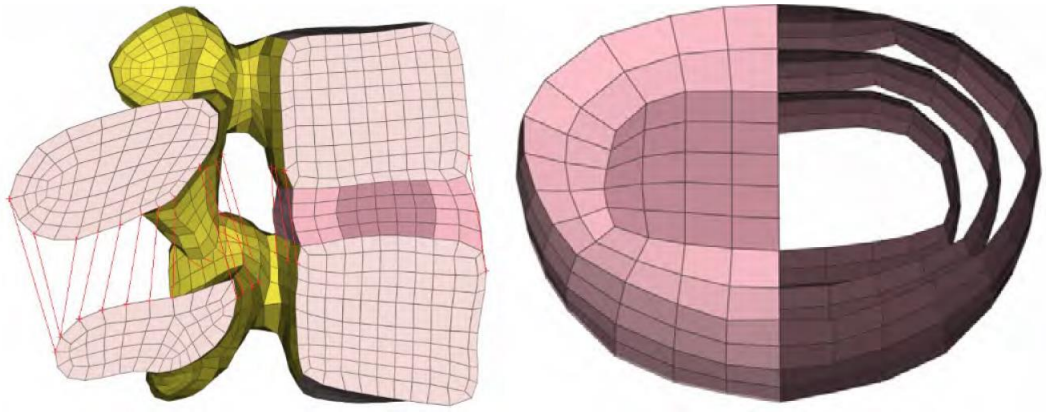

Figure 10. Exemplar mesh of the L4-L5 FSU. To the left a sagittal cross section of the vertebras and the disc is seen and to the right a vertical cross section through the disc. Half of the disc is shown with solid elements representing the nucleus and the annulus base matrix, and half of the disc with only the annulus fibers represented with shell elements. The removal of solid elements is only for illustration purposes in the figure. From (Iraeus et al., 2023).

Unknown properties were the unstretched length of the ligaments (or what spine curvature that corresponds to unstretched ligaments) and the mechanical properties of the nucleus. For the nucleus, the material parameters for an Ogden material model were tuned to match disc compression and tension experiments (Asano et al., 1992; Jamison et al., 2013; Marini et al., 2016; Markolf & Morris, 1974), see Section 3.3. Using published FSU bending tests (in flexion, lateral and torsion) (Heuer et al., 2007; Jaramillo et al., 2016), where the ligaments were removed in a stepwise manner, the contribution of and initial slack of each ligament could be quantified. To account for the initial slack, a parameter (LUMB_FLEX) was introduced in the model. Setting this parameter to 0 corresponds to a straight initial spine curvature, like an occupant seated in a normal vehicle seat. Setting it to -1 corresponds to a standing person (with a neutral lumbar spine).

The iliolumbar ligaments, located between L5 and the pelvis/sacrum were added. As no mechanical properties for these ligaments could be found in literature, these properties had to be tuned using biological experiments performed by (Yamamoto et al., 1990). For the response, see Section 3.3.

A tissue-based fracture criteria was developed for vertebral bodies. Several simulation output metrics (like stress and strain) were analyzed, and the one that best captured the compressive fractures without giving false positives e.g. during tensile loading of the spine, was the peak (over time) local inferior-superior strain measured in the trabecular part of the vertebrae body. 124 FSU tests from five PMHS test series (Brinckmann et al., 1989; Duma et al., 2006; Granhed et al., 1989; Hutton & Adams, 1982; Tushak et al., 2022) were reproduced with (scaled) simulation models representing the same FSUs. For each simulation, the peak strain was extracted at the time of fracture (in the physical test). Next, survival analysis according to (ISO/TR 12350:2013, 2013) was conducted to find the risk function that best fitted the data. The proposed injury risk function can be seen in Figure 11.

$$\text{Risk} = \frac{1}{2} + \frac{1}{2}\text{erf}\left(\frac{\ln(\text{injury criteria}) - (\beta_1 + \text{age} * \text{coef}_{\text{age}})}{\sqrt{2 * (\exp(\beta_2))^2}}\right)$$

Table III

DISTRIBUTION AND PARAMETERS FOR THE INJURY RISK FUNCTION RECOMMENDED FOR THE NEW LUMBAR SPINE MODEL

Injury risk	Injury criteria	Distribution	β_1	β_2	$coef_{age}$
Fracture	Strain	Log-normal	-2.833	-0.885	-0.0149

Figure 11. The proposed IRF to be used with the lumbar spine. From (Iraeus et al., 2023).

The injury risk function has age as a covariate and is plotted for three different ages in Figure 12.

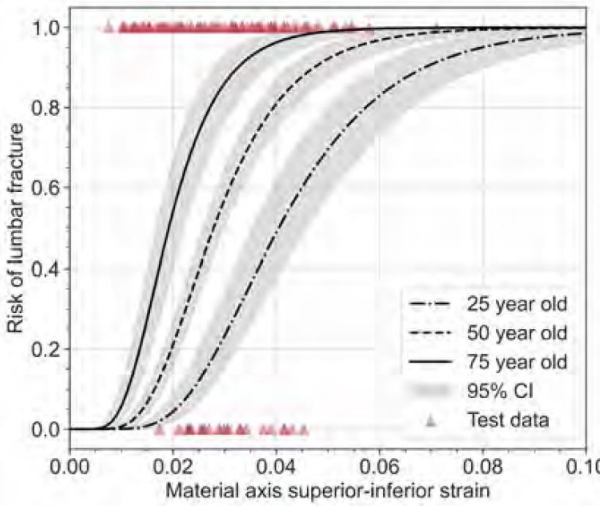

Figure 12. Proposed IRF to be used together with the updated lumbar spine model. Plotted for ages 25, 50, and 75 years of age. From (Iraeus et al., 2023).

The final step was to scale and morph the lumbar spine to fit the SAFER HBM. In this work the lumbar spine curvature from SAFER HBM version 10 was kept (which is close to the specifications from (Schneider 1983). The scaling of the lumbar spine (vertebras and discs were given the same scaling) was based on the average geometrical differences between female and male lumbar spine vertebras (Scoles et al., 1988; Zhou et al., 2000). The scaling factor in the inferior-superior direction was 1.02, while 1.11 in the other two directions. The lumbar lordosis (LL) in the final model was measured to 8.9°. This can be compared to a seated reference sample (Nishida et al., 2020), where the average LL was 1°. However, the reference data set showed a bimodal distribution (where almost no individual had a LL close to the average), and one group with “S-shaped” spine had an average LL around 8°. The LL was thus judged to be biofidelic.

2.4. Updates to the Cervical and Thoracic Spine

The thoracic and cervical spine were updated to make the spine modelling consistent for the whole spine (based on the modelling of the lumbar spine), but also to improve the overall biofidelity, and prepare the model for future updates, including fracture prediction also for the thoracic and cervical spine.

The updated thoracic and cervical spine model are based on the same average sized female geometry as the lumbar spine (Gayzik et al., 2011). The mesh strategy involves using a pure hexahedral solid (for the inner trabecular bone) and quadrilateral shell (for the outer cortical bone) mesh and using nodal connectivity to connect the vertebrae and discs, see Figure 13 (left sub figure). The end plate mesh pattern defined in the lumbar spine was consistent all the way up to T1. As the cervical vertebrae are considerably smaller than the lumbar and thoracic vertebrae, a new mesh pattern was used for the cervical spine, meaning that the connection between T1 and the lower edge of the T1 to C7 disc had to be modelled using a tied contact (LS-DYNA *CONTACT_TIED_EDGE_TO_SOLID_BEAM_OFFSET). The upper cervical vertebrae, that have different overall shape compared to the lower vertebrae, were also modelled using ANSA hexa blocks, see Figure 13 (right subfigure).

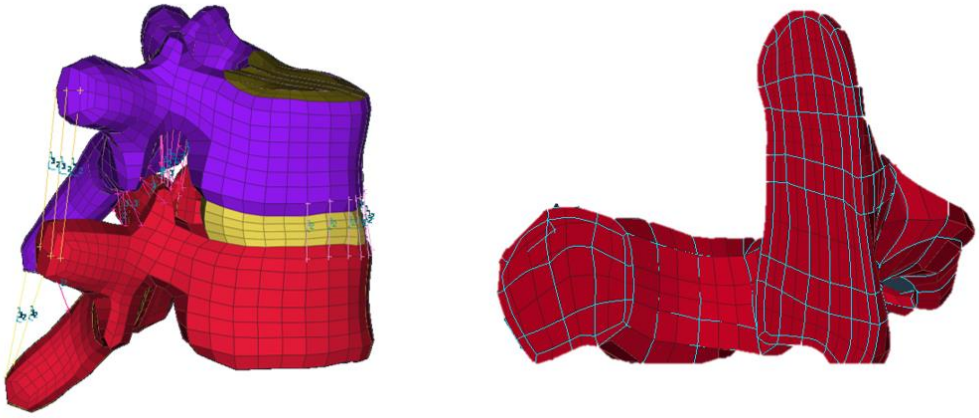

Figure 13. Left subfigure: Modelling strategy for thoracic and cervical spine shown for an FSU. Right subfigure: A closeup of the ANSA hexa block mesh strategy exemplified on the C1 vertebrae (half of the vertebrae removed to highlight the inner structure).

The thickness for the cortical shells for the cervical vertebrae (constant 0.28 mm) were based on (Ritzel et al., 1997), while the thicknesses for the thoracic vertebrae were based on (Edwards et al., 2001). The material properties for the thoracic spine are the same as for the lumbar spine, while the material properties for the cervical spine were based on; cortical bone (Reilly & Burstein, 1975), trabecular bone (Kopperdahl & Keaveny, 1998) with mineral density from (Yoganandan et al., 2006), and endplates (Wu et al., 2021).

The modelling of the intervertebral discs followed the same strategy as for the lumbar spine. The material properties for the thoracic part were based on the modelling of the lumbar spine, while the material properties for the cervical spine follows (Östh et al., 2016), except the nucleus which also for the cervical spine was based on the material properties used for the lumbar spine. The ratio of the area of nucleus pulposus to

anulus fibrosus was adjusted to be in the range of 40-50% in accordance with (Newell et al., 2017) based on the superior endplate surface area.

The ligaments for the thoracic spine were also modelled like the lumbar spine ligaments. The ligaments for the lower cervical spine were modelled using material data reported by (Mattucci & Cronin, 2015), ligament lengths and cross-sectional areas based on (Yoganandan et al., 2000), and insertion and origin points on anatomical descriptions by (Panjabi, Oxland, et al., 1991). The ligaments for the upper cervical spine were modelled based on data from (Mattucci et al., 2013), processed according to (Östh et al., 2016). All cervical ligaments except the tectorial membrane and the transverse ligaments, were modelled using beam elements. The two latter were modelled using membrane elements, to better capture the wrapping around the dens of C2.

Next the updated thoracic and cervical spine (based on an average female geometry) was scaled to fit into the SAFER HBM geometry. In this process, the transition from thoracic to cervical spine at the T1-C7 was kept constant (for the thoracic vertebrae to fit to the posterior end of the ribs), giving an additional constraint to the superior-inferior scaling. For the thoracic spine the scaling was based on a statistical shape model of the thoracic spine (Lian et al., 2023). This gave a superior-inferior scaling factor of 1.060 and a horizontal scaling factor of 1.140. The scaling for the cervical spine was done to fit the spine inside the SAFER HBM and resulted in a superior-inferior scale factor of 1.097 which was also used for horizontal scaling. The scaled dimensions were also cross checked to other published data (Busscher et al., 2010; Panjabi, Takata, et al., 1991). Finally, the scaled spine was morphed to fit the original curvature of the SAFER HBM.

2.5. Updates to the Clavicula, Scapula and Humerus

The updates to the clavicula, scapula and humerus were done to prepare these bones for tissue-based injury risk assessment. The mesh was created based on the same average sized female geometry as was used for other body parts in this report (Gayzik et al., 2011). Also, like the other bones an ANSA hexa block mesh strategy was adopted to ensure high quality, all hexahedral elements. However, as the cortical bones of these three bones are generally thicker than for example the thinnest part of the pelvis and the ribs, also the cortical bones were modelled using solid elements. One layer of solid elements was used to represent the cortical bone everywhere, see Figure 14 and Figure 16, except for the humerus shaft, that has thicker cortical bone. Here, two layers of solid elements were used for the cortical bone, see Figure 15. While the middle part of the humerus shaft does not contain any trabecular bone (contains bone marrow instead), also this part was filled with solid elements with trabecular bone properties. As the scapula is very thin for most parts of the fossa, it was hypothesized that this part only consists of cortical bone. Trabecular bone was thus only modelled at the bulkier inferior-lateral edge of the main fossa, partly seen in Figure 16, and at the inner part of the also bulkier scapulae spine.

The material properties for the cortical bones (all three bones) were based on data for wet humeral bone (Nahum & Melvin, 2012), modelled using an isotropic elastic-perfectly plastic material with the Young's modulus set to 17.2 GPa, and the yield

stress to 123 MPa. The material properties for the trabecular bone were based on indentation test of the distal humerus presented in (Dunham et al., 2005). Also, the trabecular bone was modelled by using an isotropic elastic-perfect plastic material model, with Young's modulus of 0.31 GPa, and yield stress of 4.4 MPa.

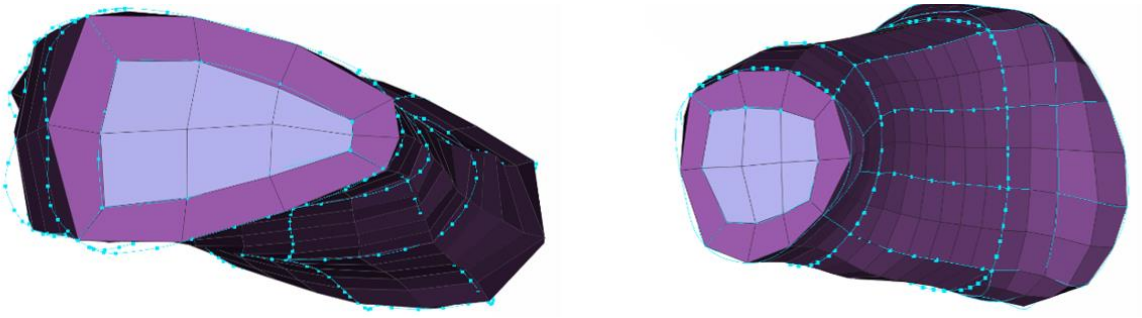

Figure 14. The mesh of the clavicula, left lateral end and right medial end. The blue lines are the edges of the ANSA hexa blocks.

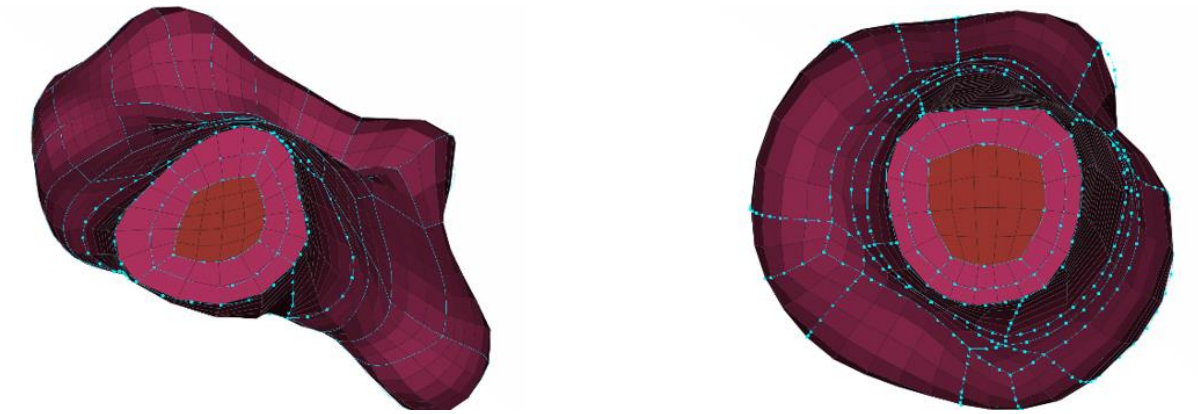

Figure 15. The mesh of the humerus (left) distal end and (right) proximal end. The blue lines are the edges of the ANSA hexa blocks.

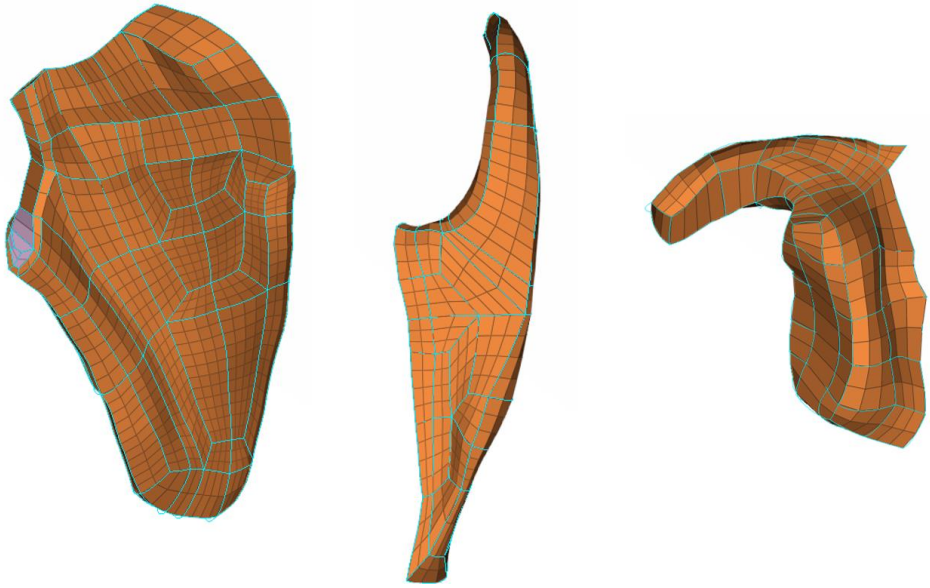

Figure 16. The mesh of the scapula. Left the main part of the scapula (infraspinousus and subscapular fossa), middle the acromion, and right the coracoid process and glenoid cavity. The blue lines are the edges of the ANSA hexa blocks.

To adapt the bones to fit the SAFER HBM, geometry scaling was used. First volumetric scaling using a scaling factor of 1.09 was used for all three bones. This factor roughly corresponds to the ratio of average male to average female stature. Per definition of volumetric scaling (of solid elements) this procedure scales both the length, cross section and thickness of the cortical bone. No more scaling was done to the scapula, as suitable references were not found to further enhance this scaling.

However, to fit the other two bones into the SAFER HBM, the length of the clavicle and humerus had to be changed (to fit to the already existing body structures). This was done by morphing the shaft regions of these two bones, along the longitudinal axes. This procedure changes the overall length but did not change the cross section or cortical thickness.

The clavicle in the final model measures 167 mm (measured as the length of the long side of a box enclosing the clavicula). This is within one standard deviation (161.9 ± 10.4 mm) of the average length of a dataset (n = 20) measuring subjects with an average stature of 175 mm (Lu & Untaroiu, 2013). The same dataset was also used to verify the cross-sectional area after scaling, which is presented in Figure 17. All along the clavicle, except for two points close to the lateral end, the clavicle model falls within the 1 SD range of the measured data.

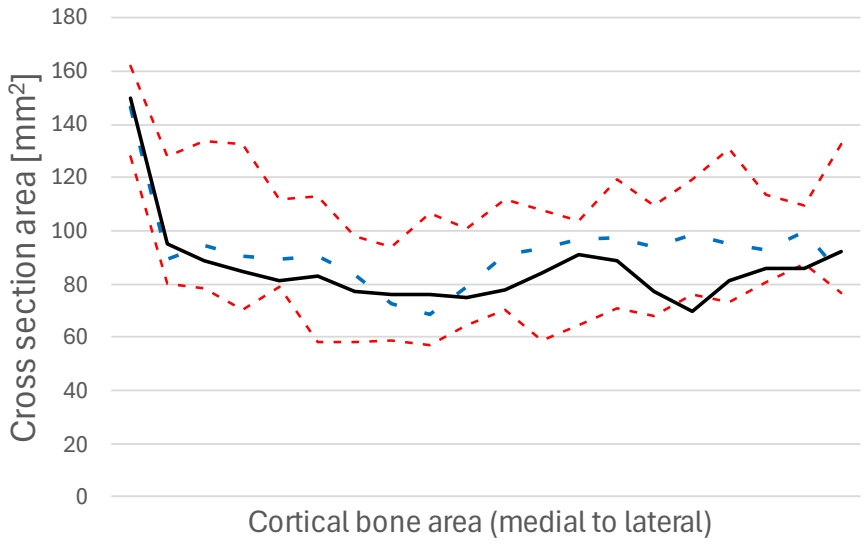

Figure 17. Verification of clavicle cortical bone area to (Lu & Untaroiu, 2013). The blue and red lines correspond to the average and standard deviation of the physical measurements, while the black line represents the clavicle model after scaling.

The humerus in the final model measures 350 mm. However, it is compared to published results using another measurement "biomechanical length" (BML), which according to (Drew et al., 2019) is defined as "distance along the Z-axis between the humeral head center and the mid-point of the distal cylindrical axis". The Drew et al study included pairs of humeri from 43 male donors of unknown stature. The BML length in the model is 317 mm, which is within 1 SD of the reported length for males 298.3 ± 24.5 mm in the aforementioned study. The same study also reported average

cortical thickness at five locations along the bone. The average humeral cortical thickness in the model is compared to the Drew et al. data in Figure 18. The cortical thickness in the model is within the 1 SD corridor for the whole shaft length.

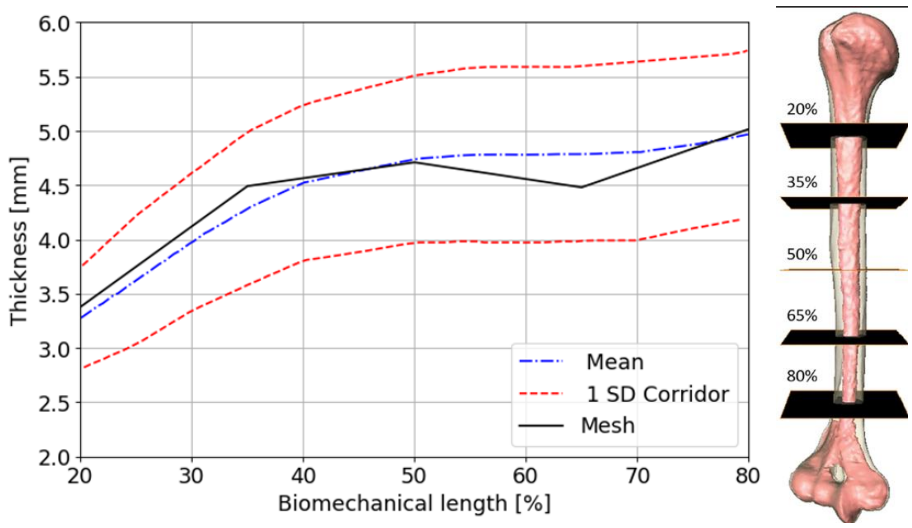

Figure 18. Average cortical thickness for the humerus, compared to (Drew et al., 2019). The blue and red lines correspond to the average and standard deviation of the physical measurements, while the black line represents the clavicle model after scaling.

2.6. Updates to the Costovertebral joints

The costovertebral joints were updated to connect the updated thoracic spine to the ribs. The costovertebral joints were updated by first creating and tuning a prototype joint at rib level 6. The joint modelling loosely follows the procedure outlined in (Aira et al., 2019).

First, the posterior end of the rib was locally morphed to fit the shape of the vertebrae transverse process, see Figure 19 (right). Next, ligaments were modelled between already existing nodes according to Figure 19 (left). For the radial ligament (CRL) eleven beam elements with a total area of 46 mm^2 were added, see Table 2. Similarly, for the Intraarticular (CIAL)/Transverse superior (CTSL)/Transverse (CTL)/Lateral Transverse (CLTL) ligaments 2/4/12/3 beam elements with a total area of 3.2/19.0/42.0/10.2 mm^2 were added. As no literature data was available on the material properties for these ligaments, material parameters (assumed to be a bilinear response like many other ligaments) were tuned based on experiments performed by (Duprey et al., 2010). The resulting material parameters can be seen in Table 2, and the tuned stiffness of the joint in Section 3.6.

Table 2. Cross sectional geometry and material properties for the costovertebral joints.

		Tot area	ε_{toe}	E_{toe}	E_{lin}
	NEL	[mm2]	[-]	[GPa]	[GPa]
Radial ligament	11	46.4	0.049	0.02	1.12
Intraarticualar ligament	2	3.2	0.049	0.02	1.12
Transverse superior ligament	4	19.0	0.085	0.05	1.44
Transverse ligament	10	42.0	0.085	0.05	1.44
Lateral ligament	3	10.2	0.085	0.05	1.44

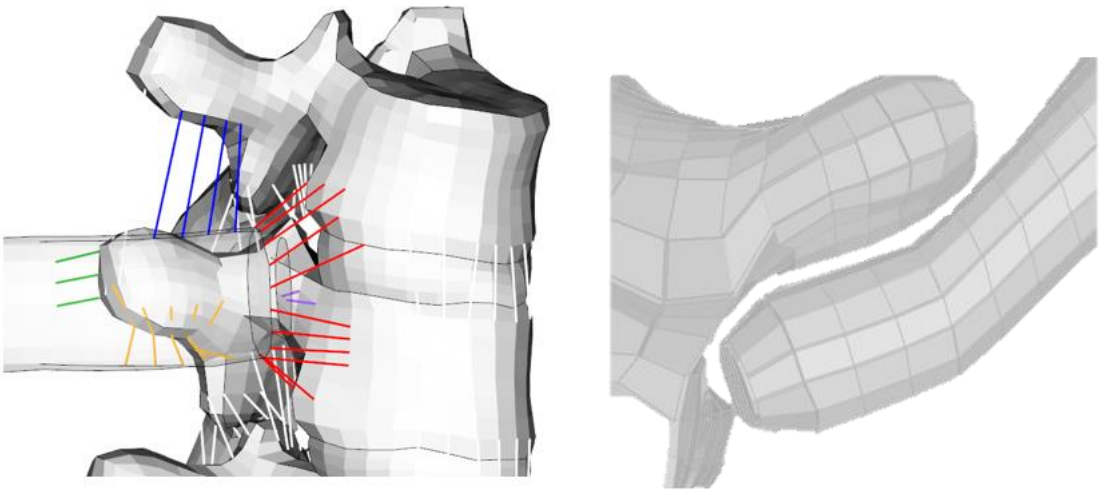

Figure 19. The updated costovertebral joint consists of five ligaments per rib, red=radial ligament, purple=intraarticular ligament, blue=transverse superior ligament, orange=transverse ligament, and green=lateral transverse ligament. The posterior rib ends were morphed to fit closely to the vertebrae transverse processes.

The modelling strategy for rib level 6 was copied to all costovertebral joint locations, see Figure 20 (left). All joints except for levels 1, 11 and 12 were modelled identical. For levels 1, 11 and 12 the Transversal Super Ligament (TSL) was removed, and the Radial Ligament (RAL) was only connected to the ego (corresponding to the same rib level) vertebra, see Figure 20 (mid and right).

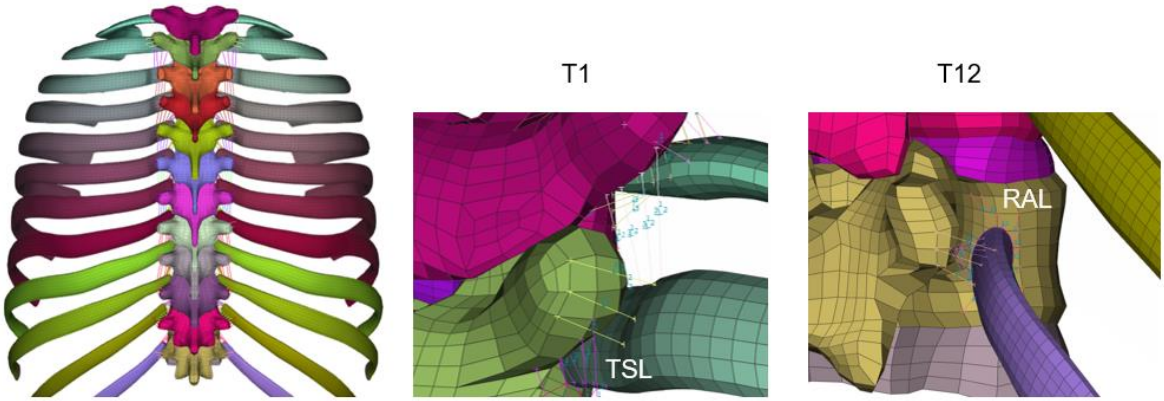

Figure 20. The complete thoracic spine updated according to the prototype joint defined in Figure 19. T1, T11 and T12 had to be modelled slightly differently. For these ligaments the Transversal Superior Ligament (TSL) was removed, and the Radial Ligaments (RAL) was only connected to the ego vertebrae.

2.7. Updates to the Soft tissues

The soft tissue was updated to enhance mesh quality, improve overall biofidelity, to allow for population-based variations in BMI through morphing, and specifically for the hip to improve submarining prediction. The updates to the soft tissues, from the rib level twelve down to the knee, have been described in detail in (Brynskog et al., 2024a). In summary, the target surface for the new geometry of the skin, covering the hip and thighs of the SAFER HBM, was based on the HumanShape™ (www.humanshape.org) data (Park et al., 2022), downloaded on 22 August 2022. An outer contour of a target

male subject was collected in a seated posture with anthropometric variables set to the baseline for the SAFER HBM (age = 45 years, stature = 1750 mm, weight = 77 kg), and a sitting height to stature (SHS) ratio = 0.52). The surface was then aligned by matching the human shape H-point with the H-point of the SAFER HBM. However, due to how the outer skin data was collected, some modifications were made to the surface. These include aligning the leg position, shaping the buttock to represent an unloaded subject (since the scans were made on a rigid seat), and adding an abdomen fold in the abdomen-thigh transition (since this was smoothed by the mesh fitting algorithm in the HumanShape™ data), see (Brynskog et al., 2024a). Using the outer skin surface, hexa blocks were constructed in ANSA to generate a full hexa mesh of the soft tissues surrounding the hips and thighs.

To have a computationally efficient model, the SAFER HBM does not target models of individual 3-D muscles. Instead, fat and muscle material properties were separately assigned to volumes of the soft tissue mesh that approximates the fat/muscle distribution, defined based on anatomical textbooks, see Figure 21. The muscle volumes considered include the gluteal muscles, the inferior aspect of the erector spinae, and the thigh muscles. The fat material was implemented as an Ogden model using reported parameters for average fat stiffness (Naseri, 2022) while the muscles material utilized a stiff fat representation (Naseri, 2022), lacking a robust material model validated from muscle tissue in relevant loading scenarios.

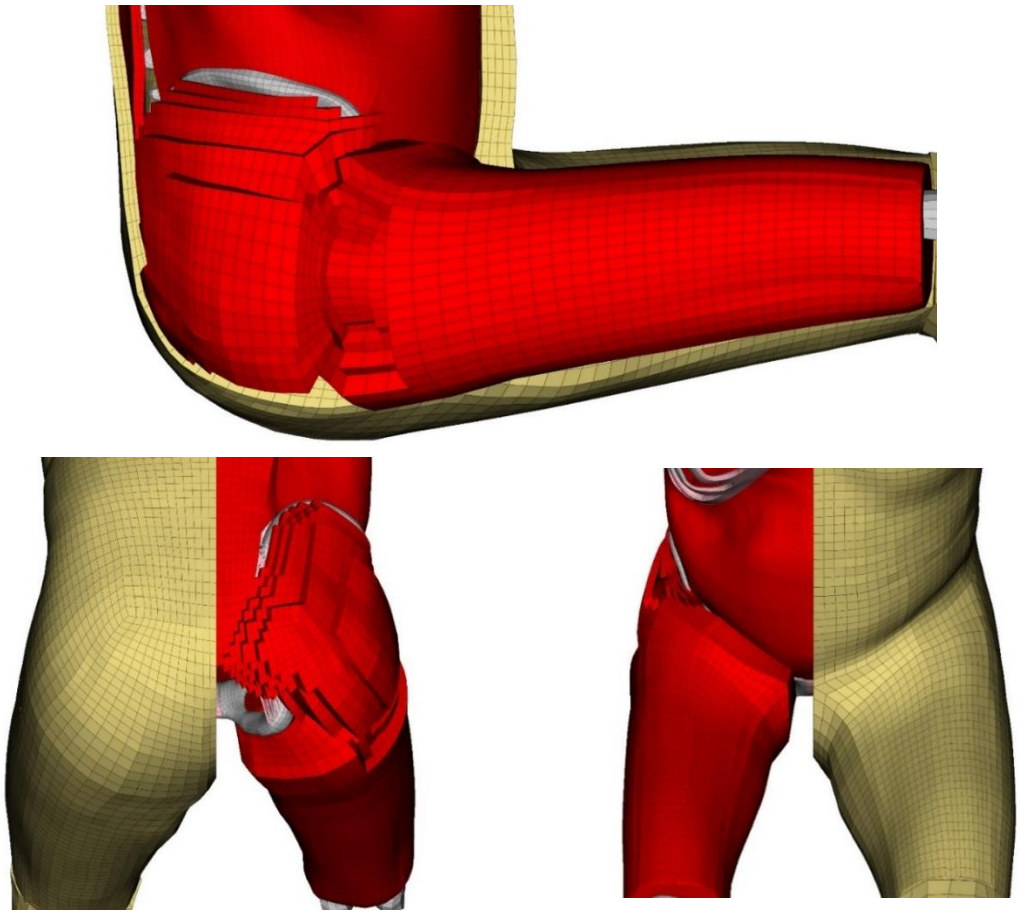

Figure 21. Fat (beige) / muscle (red) distribution around the thigh and buttocks. The apparent voids seen in the figure are filled with fat tissue elements.

The thigh muscle elements adjacent to the femur surface have been tied all along the femur shaft, while the elements representing the hip muscles have been connected to the pelvis model at areas approximately matching their origin/insertion. The pelvis-to-hip muscle connection was achieved by extruding a one element thick solid layer which shares nodes with the skeleton on one side and was surface aligned and tied to the muscle elements using a contact (*TIED_NODES_TO_SURFACE_OFFSET in LS-DYNA) on the other side, see Figure 22. The muscle attachment elements were given material properties based on high-speed tension tests on human thigh muscles (Zhai et al., 2019).

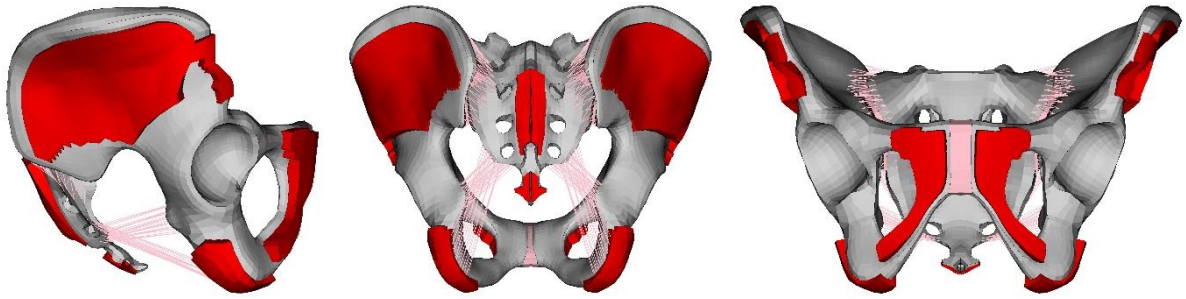

Figure 22. Muscle attachment elements for the pelvis.

Similarly, the soft tissues around the lumbar spine was morphed to give a snug fit to the updated lumbar spine, and the abdominal insert (representing abdominal organs) were attached to the anterior aspect of the vertebras, see Figure 23, using a combination of extruded solid elements and a tied contact (*CONTACT_TIED_NODES_TO_SURFACE_OFFSET in LS-DYNA), similar to above. The material parameters for the solids were based on (Zhai et al., 2019).

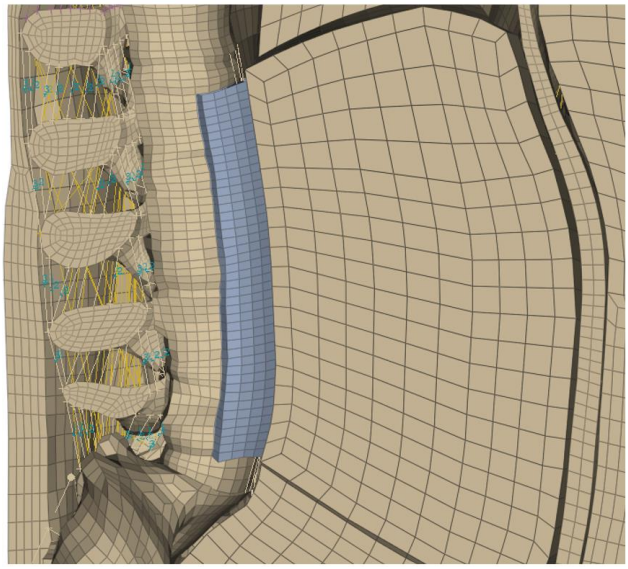

Figure 23. The anterior part of the lumbar spine (L2 to L5) was connected to the abdominal insert using one row of elements, offset from the lumbar spine, and tied to the abdominal insert using a tied contact.

Also, for the cervical and thoracic spine, the surrounding soft tissues were locally morphed to give a snug fit around the updated spine, and all discrete muscle elements

were reattached, see *Figure 24*. The thoracic spine was connected to the internal organs using the same modelling strategy as shown for the lumbar spine in Figure 23.

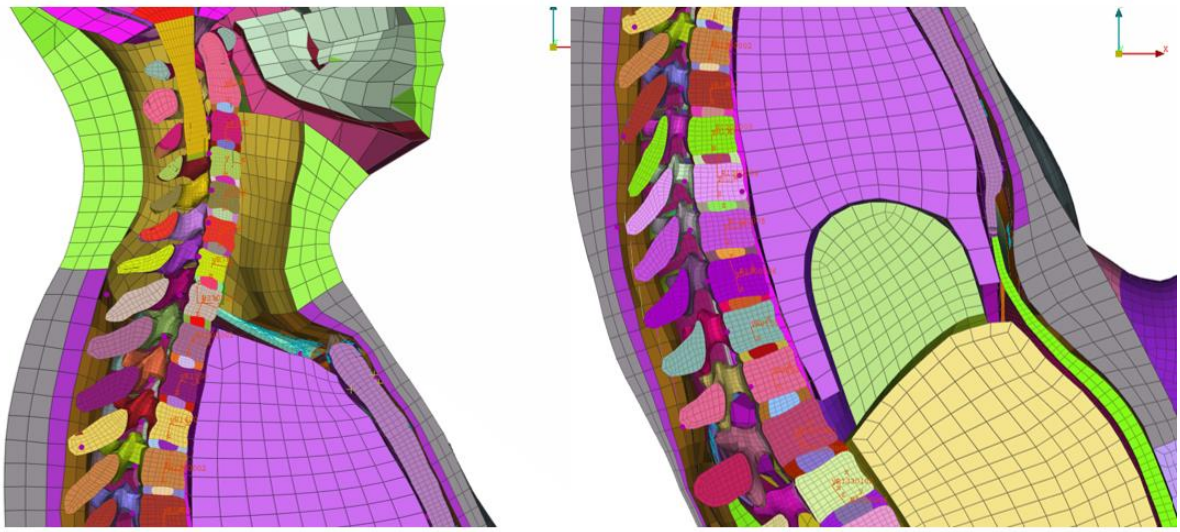

Figure 24. The new cervical and thoracic spine integrated into the SAFER HBM. The visibility of the discrete muscle elements attached at various vertebrae is turned off to make the figure clearer. Please note the coordinate system in each vertebra, used to define the local material axes for the anisotropic trabecular bone.

One exception to the muscle modeling strategy described above was made by the introduction of an explicitly modeled abdomen muscle wall, connecting the ribcage with the pubis rami and the iliac crest, see Figure 25. The geometry for the muscle wall was created by projecting the HumanShape™ skin surface using subcutaneous adipose tissue (SAT) thickness data (Holcombe & Wang, 2014) and targeting an average male rectus abdominus muscle thickness of ~10 mm and a lateral abdominal thickness of ~18 mm (Tahan et al., 2016). A full hexa/quad mesh was then generated using hexa blocks in ANSA. The solid elements were modelled as constant stress solids (ELFORM = 1 in LS-DYNA) with material properties from a stiff fat model (Naseri, 2022).

A no-separation sliding-only contact (*AUTOMATIC_SURFACE_TO_SURFACE_TIEBREAK with OPTION = 4 in LS-DYNA) was modeled between the abdomen muscle wall and the abdomen subcutaneous fat on one side, and between the abdomen muscle wall and the abdominal cavity volumes, on the other side. This was implemented to replicate fascia, connecting the muscle and fat but allowing relative movement.

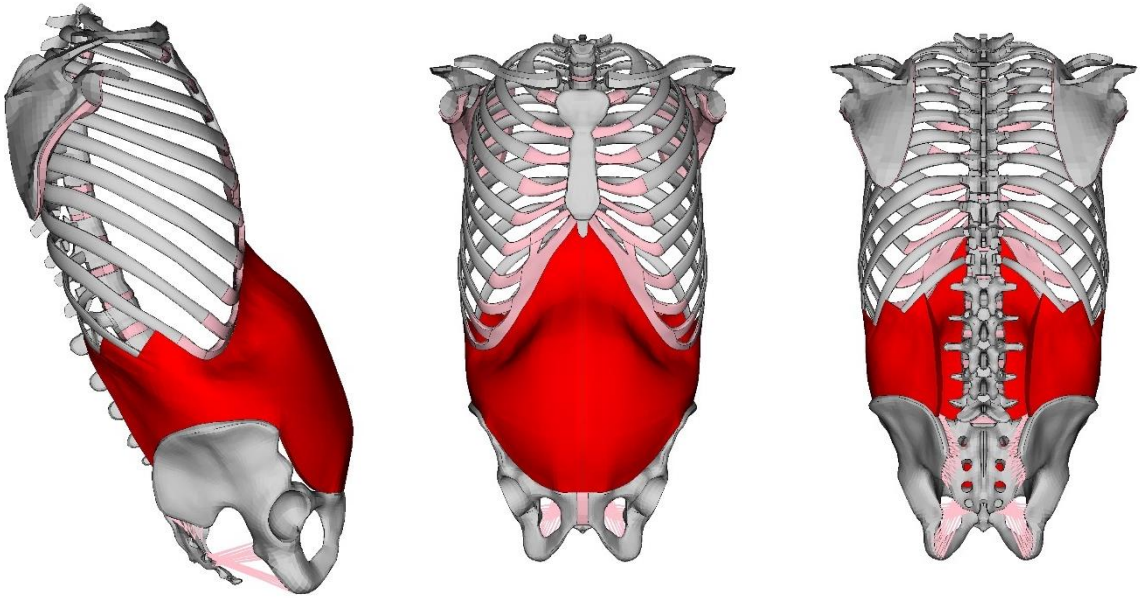

Figure 25. New abdomen muscle wall (red) connecting the pelvis and the ribcage.

To fill the new abdomen/pelvic cavity, and improve the overall mesh quality, the lower abdomen and pelvic cavity volumes were re-meshed, see Figure 26. To couple the meshed volumes with each other, the no-separation sliding-only contact was also implemented between the lower abdomen and pelvic volumes. The material properties of these volumes were also updated to the stiff fat model (Naseri, 2022).

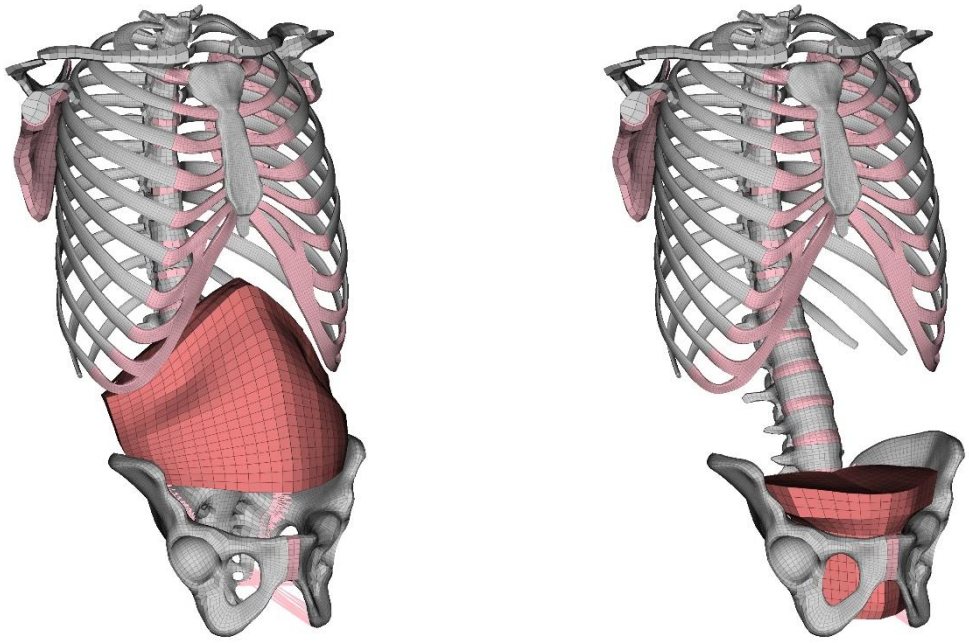

Figure 26. Re-meshed lower abdominal cavity volume (left) and pelvic cavity volume (right).

For the upper abdominal cavity and the lungs, the mesh was adequate, and only the material was updated. The material model for the lungs were changed to *MAT_LOW_DENSITY_FOAM with parameters according to (Rater, 2013), see Figure 27 (right). The upper abdominal cavity material was changed to the stiff form of fat tissue according to (Naseri, 2022), see Figure 27 (left).

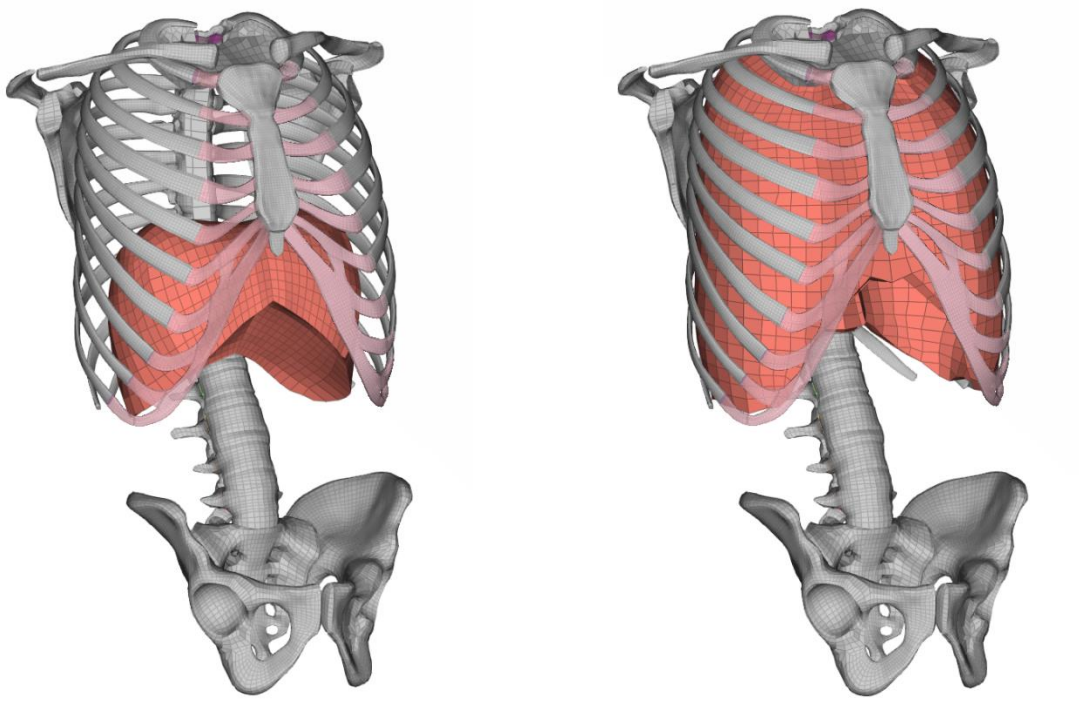

Figure 27. The upper abdominal cavity (left) and the lungs (right) were given new material models.

To close the inferior opening of the bony pelvis model, the pelvic floor was modelled using fully integrated shell elements, where the shells bridge the pubis, ischial spine, coccyx, and sacrum, see Figure 28. Since the pelvic floor acts as a support for the pelvic organs, the shells were tied (*TIED_NODES_TO_SURFACE_OFFSET in LS-DYNA) to the bottom nodes of the pelvic cavity volume. The average thickness of puborectalis and iliococcygeus has been estimated at 5.9 mm in men (Stansfield et al., 2023) and was used for all pelvic floor elements. A linear elastic material model with an elastic stiffness of 1 MPa was estimated from the high-speed muscle tension tests by (Zhai et al., 2019).

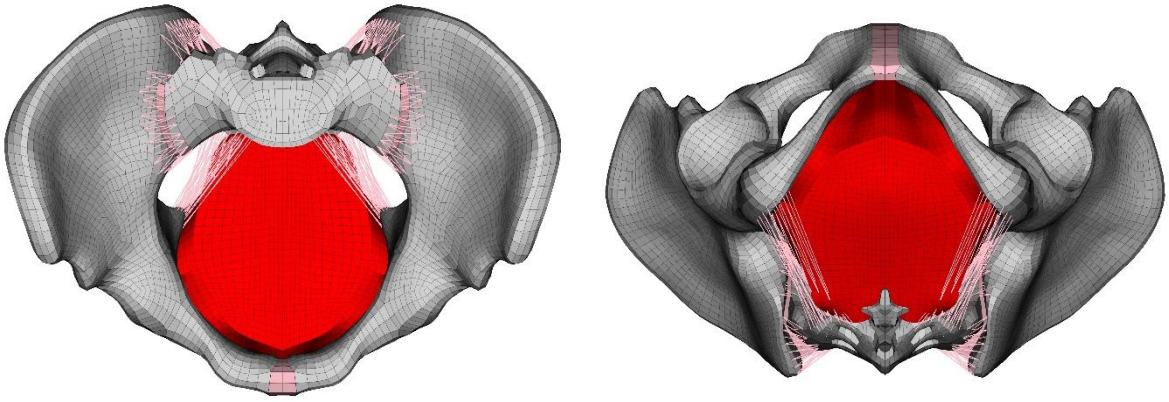

Figure 28. Shell representation of pelvic floor muscle from superior view (left) and inferior view (right).

In addition, the soft tissues of the lower leg were remodeled, with the inner surface based on the lower leg bones introduced in SAFER HBM v10. Here, the soft tissue was not separated into fat and muscle tissue (as for the upper leg), see Figure 29 (left). The soft tissue mesh can be seen as a sleeve around the tibia, fibula and the bones of the

foot, and the nodes are tied to the bones using (*TIED_SHELL_EDGE_TO_SURFACE_BEAM_OFFSET in LS-DYNA). The material parameters for the lower leg were based on (Hedenstierna, 2008), while the soft tissue of the foot was based on the stiff form of adipose tissue in (Naseri, 2022).

The soft tissues of the lower arm were also updated, see Figure 29 (right). As the ulna and radius can move relative each other during pronation and supination, the mesh pattern was outlined "twisted", to follow the two bones (as positioned in the base model). Like other body regions, the soft tissue mesh of the lower arm was attached to the bones, to the hand and to the upper arm, using tied contacts (*TIED_SHELL_EDGE_TO_SURFACE_BEAM_OFFSET in LS-DYNA). The material parameters for the lower arm were also based on (Hedenstierna, 2008).

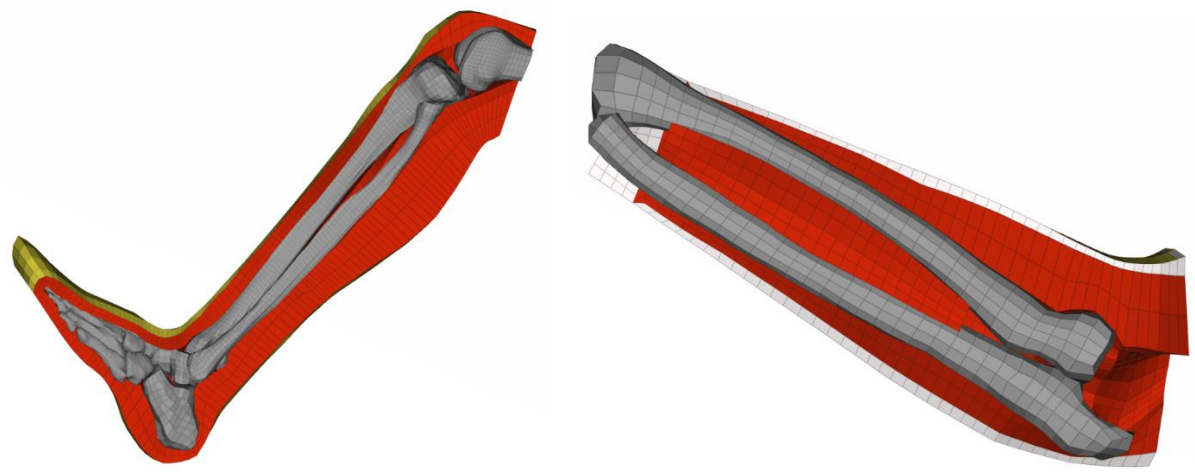

Figure 29. New soft tissue meshes of the lower leg (left), and the lower arm (right). Red elements represent muscle tissue and white elements fat tissue.

2.8. Update of the Muscle Elements

The scapulae of the SAFER HBM are held in place on the thorax by several one-dimensional elements representing the rhomboideus, the serratus anterior, and the lower parts of the trapezius, see Figure 30. These were modelled using *ELEMENT_DISCRETE and *MAT_SPRING_MUSCLE in SAFER HBM version 10, which requires the initial length of the muscle (L_0) to be known prior to simulation. This creates issues when repositioning and morphing the model, as the L_0 must be updated manually to match the updated length of the muscle. For SAFER HBM version 11, all *MAT_SPRING_MUSCLE elements and their colinear damping elements were converted to *MAT_MUSCLE with parameters identified such that equivalent element properties were achieved.

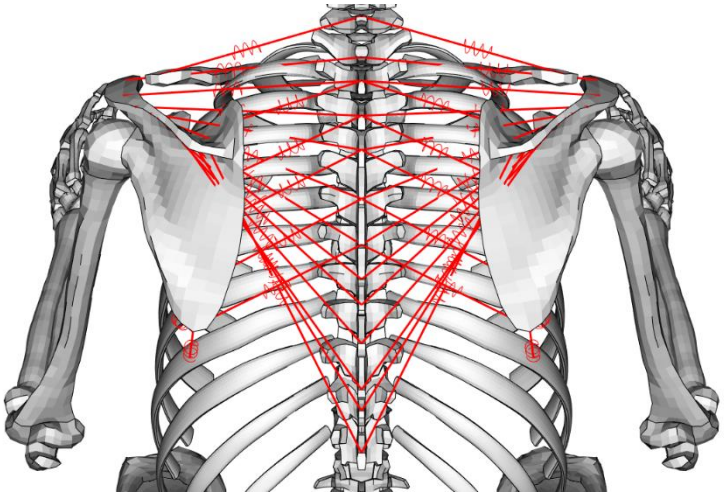

*Figure 30. Muscles that were updated from *ELEMENT_DISCRETE to *ELEMENT_BEAM and *MAT_MUSCLE for SAFER HBM v11.*

To make the muscle routing of the muscles used by the active HBM feedback control more biofidelic, six cervical spine muscles and two lumbar paravertebral muscles were rerouted using soft tissue or skeletal via points. For the cervical spine, Figure 31, the sternocleidomastoid, the trapezius, the levator scapulae, the splenius capitis, the splenius cervicis and the erector spinae longissimus capitis muscles span the whole length of the cervical spine was rerouted through the soft tissue mesh using the keyword *PART_AVERAGED. These updates have previously been reported in (Larsson et al., 2023).

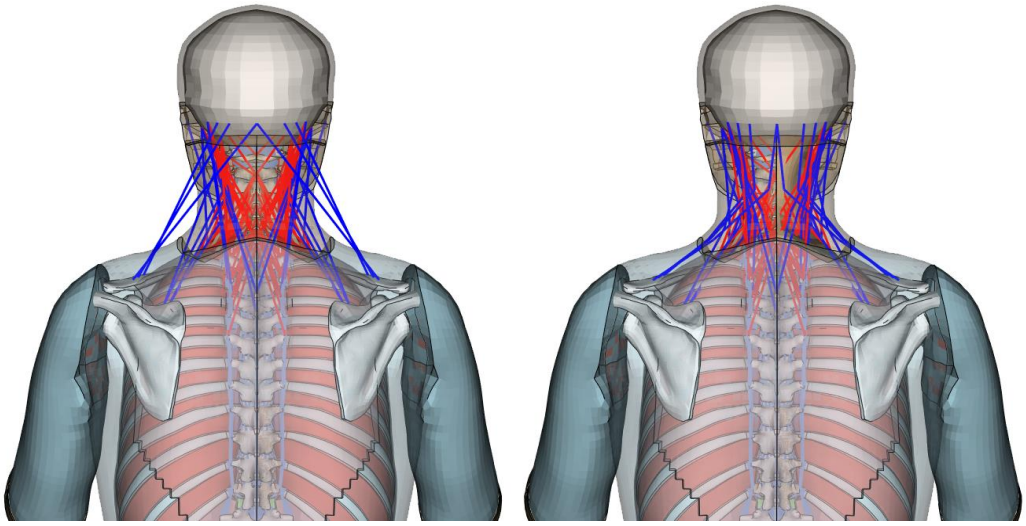

Figure 31. Left: cervical muscles before rerouting (SAFER HBM v10). Right: cervical muscles after rerouting of the trapezius, levator scapulae, splenius capitis, splenius cervicis and erector spinae longissimus capitis muscles (blue) for SAFER HBM v11.

For the lumbar spine the fascicles of the erector spinae spanning from the pelvis to the rib cage were re-routed using via points on the ribs, see Figure 32.

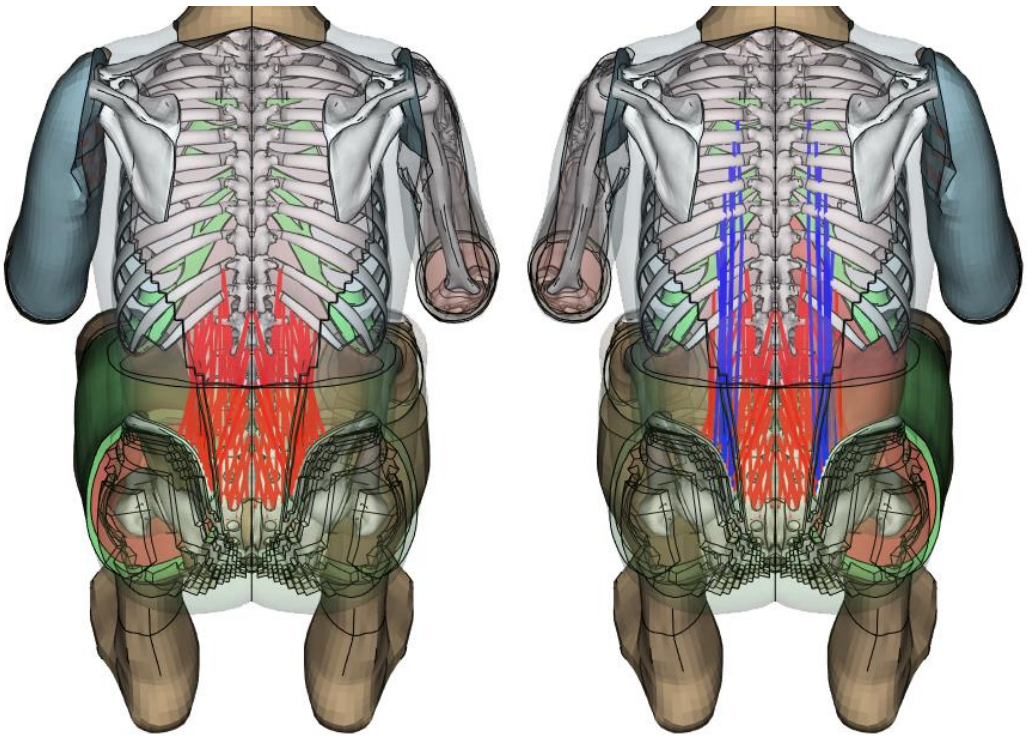

Figure 32. Left: lumbar paravertebral muscles before rerouting (SAFER HBM v10). Right: lumbar paravertebral muscles (blue) after rerouting of the erector spinae longissimus for SAFER HBM v11.

2.9. Model renumbering

The whole model was renumbered, and fitted into a smaller number range, to enable the use of several SAFER HBMs in one vehicle model, while keeping the total HBM entities within a 10M range.

Identifiers for parts, materials, sets, and others now follow a 6-digit numbering scheme, where the digits indicate the position of the part with respect to the human body and with respect to adjacent parts. For the numbering scheme, SAFER HBM version 11 is divided into 6 body regions (head, neck, upper extremity, thorax, abdomen and pelvis, and lower extremity). These body regions are each given a separate range, indicated by the first digit of the identifier. Parts associated with the muscle implementation are given a separate range (300000). The identifiers are numbered from cranial to caudal/distal and/or medial to lateral directions. For example, in the upper extremity, clavicle and scapula take a lower number than the phalanges of the hand.

The naming of the parts includes Body Region and the anatomical name in Latin name, with the words concatenated with an underscore (_). The part name ends with the sagittal aspect if there are symmetric components ("_Left"/"_Right"), giving the possibility that parts on both sides can be selected in a preprocessor by searching of the name of the component leaving out the ending "_Left"/"_Right"

Table 3. The numbering rules that are used for SAFER HBM version 11.

Rubric						
Place	***x*00000**	***0x*0000**	***00x*000**	***000x*00**	***0000x*0**	***00000x***
Place Description	Body region/ subsystem	Sagittal aspect	Major part (optional)	Major part	Minor part	Used only when several subparts are required
Value notation/ description	**3** – Muscle **4** – Head **5** – Neck **6** – Upper Extremity **7** – Thorax **8** – Abdomen and Pelvis **9** – Lower Extremity	**0** – Parts on the mid-sagittal plane If a part has symmetry counterpart, then, **1** – Left **6** – Right	This place is optional and used in addition or combination with the 4th digit for parts requiring additional digits in the numbering series, for e.g., thoracic spine which has 12 levels	This place is used for major parts. Gaps in the numbering are given by design to accommodate expansion from future developments.	This place is used to identify components within the major part	This place is used when repetitive structures or additional sub-parts are required for an organ or part.

Some examples:

8**0**0300 – Abdomen_Pelvis_Sacrum_Cortical (Sacrum takes the value 0 here since it lies on the mid-sagittal plane)

80**13**30 – Abdomen_L3_Trabecular (L3 vertebra takes the number 13 at this place and hence use the 3rd and 4th digit.)

801331- Abdomen_L3_Trabecular_Posterior (In this case, the last digit is used for the posterior part of the vertebra)

801161 - Abdomen_L1-L2_Interbertebral_Disc_AF_Fibers_In_1 (Number 1-6 (1 in the example) at the last position indicate the 3 pairs of annular fiber layers.

9**1**0380 - Lower_Extremity_Fibula_Trabecular_Left (Left fibula takes the value 1, while the right fibula takes 6. (All parts symmetric about sagittal plane are offset by 50000))

9**6**0380 - Lower_Extremity_Fibula_Trabecular_Right

3. Model Tuning and Validation

As of SAFER HBM version 11, all validations have been collected in a validation repository on GitHUB. In this repository the validations are presented using Jupyter Notebooks, with simulation results post processed using the DYNASAUR post processor. In this chapter, the validation that has been carried out to verify the updates of SAFER HBM version 11 will be presented. If the validation is already included in the validation repository, it will be referenced with a short introduction. Some validation load cases are not yet in the repository, and those will be presented with results in this report.

3.1. Pelvis Tuning and Validation

At the time of pelvis bone development, there was a lack of published material properties for the pubis symphysis (PS) joint. Due to this the joint was modelled using a rubber material model with stress-strain response calibrated against component tests by (Dakin et al., 2001), to match the average tension/compression response, see Figure 33. Details are provided in (Brynskog et al., 2022)

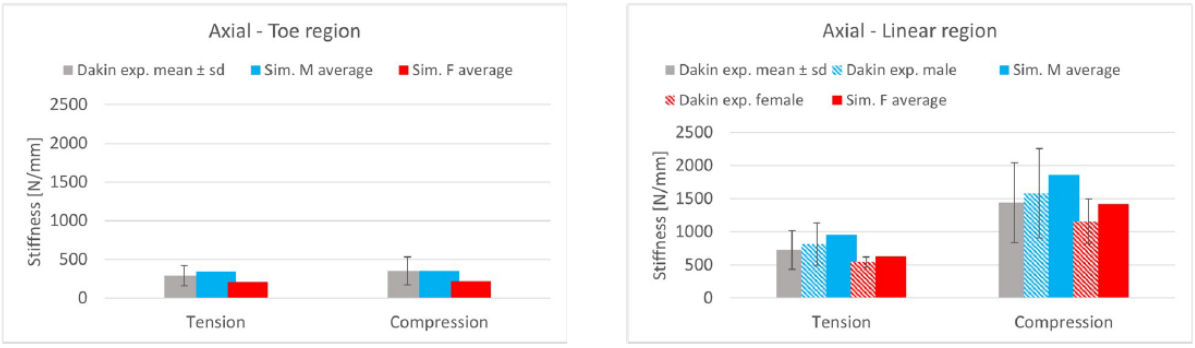

Figure 33. The resulting PS joint stiffness in tension and compression. From (Brynskog et al., 2022).

The same tuned material parameters were also used for the Sacroiliac (SI) joint, lacking alternative data. The evaluation of the SI joint stiffness is seen in *Figure 34*.

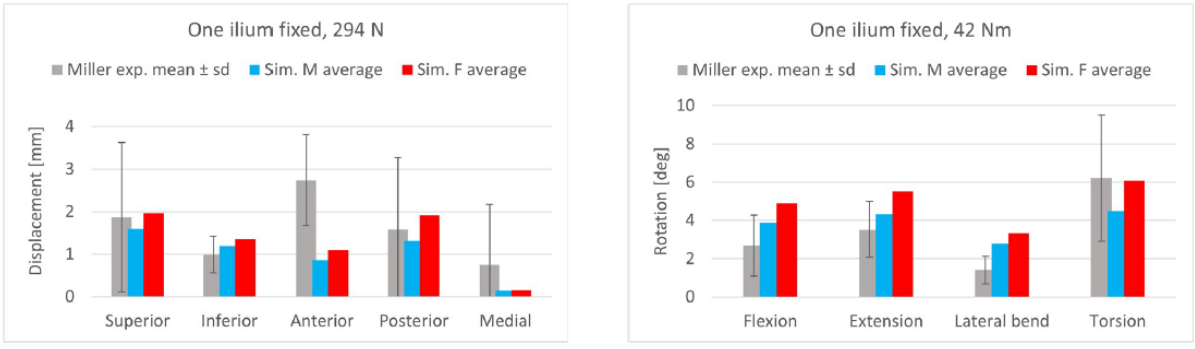

Figure 34. The resulting SI joint stiffness in various loading conditions. From (Brynskog et al., 2022).

Component level validation of the pelvis FE-model was done against quasi-static and dynamic lateral loading experiments performed by (Guillemot et al., 1998), and have been published in (Brynskog et al., 2022). These validations are available in the validation repository for SAFER HBM v11.

3.2. Femur Validation

The femur model kinetic and kinematic responses were validated to the combined axial load and 3-point bending tests presented in (Ivarsson et al., 2009) and have previously been reported in (Svensson, 2022). This validation is also available in the validation repository for SAFER HBM v11.

3.3. Lumbar Spine Tuning and Validation

Using the step-wise reduction studies published by (Heuer et al., 2007; Jaramillo et al., 2016), it was shown that initial pre-stretch/slack had to be defined to the ligaments; -1.5 mm for ALL, +1.5 mm for PLL, +2.0 mm for FC and FL and +5.0 mm for ISL and SSL. This corresponds to a pure rotation around the FSU center or rotation (approximately 2/3 from the anterior edge of the disc). The joint stiffness after adding this slack can be compared to the (Heuer et al., 2007; Jaramillo et al., 2016) data in Figure 35.

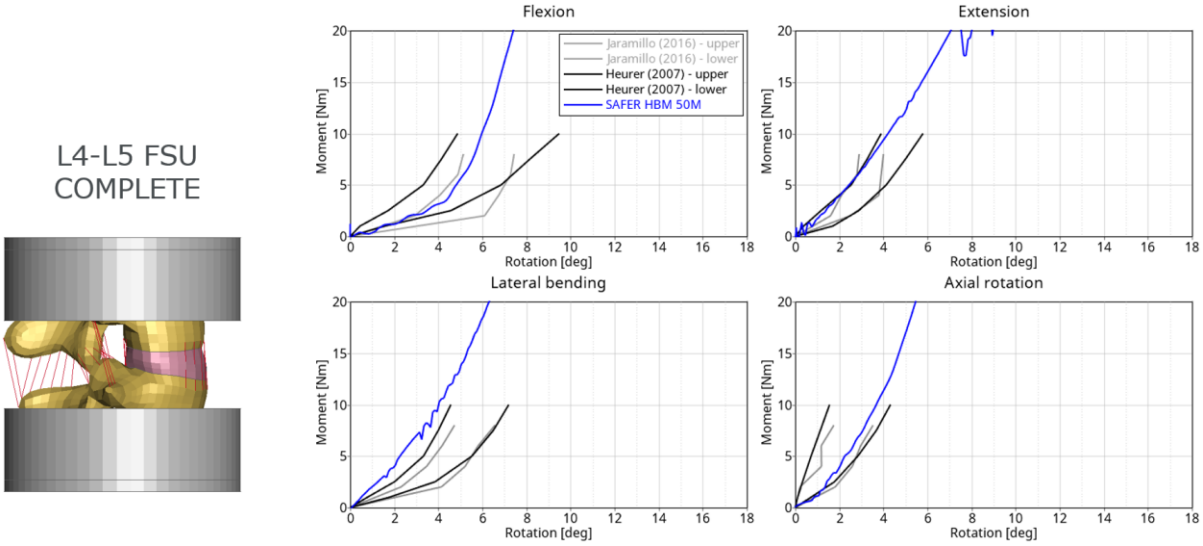

Figure 35. The resulting stiffness of the L4-L5 FSU in flexion, extension, lateral bending and axial rotation for the updated lumbar spine after tuning the initial slack of ligaments.

The kinetic and kinematic response of the whole lumbar spine was validated to two isolated lumbar spine PMHS tests (Demetropoulos et al., 1998; Yamamoto et al., 1989), where the lumbar spine was subjected to flexion, extension, lateral bending and torsional moments, and have previously been presented in (Iraeus et al., 2023). This validation is also available in the validation repository for SAFER HBM v11.

In Figure 36 the effect on the joint stiffness of removing the ILIO ligament on one or two sides can be seen. According to (Yamamoto et al., 1990) the bilateral removal of the ILIO ligament should give an additional 1.7° rotation in flexion which is similar to the model prediction. For lateral bending Yamamoto et al. measured 1.1° additional rotation when bilaterally removing the ILIO ligaments. The model predicts 2.2° additional rotation and is thus too flexible. In axial rotation Yamamoto et al. measured 0.3° additional rotation, while the model predicts 0.15°, making the model too stiff in this load case.

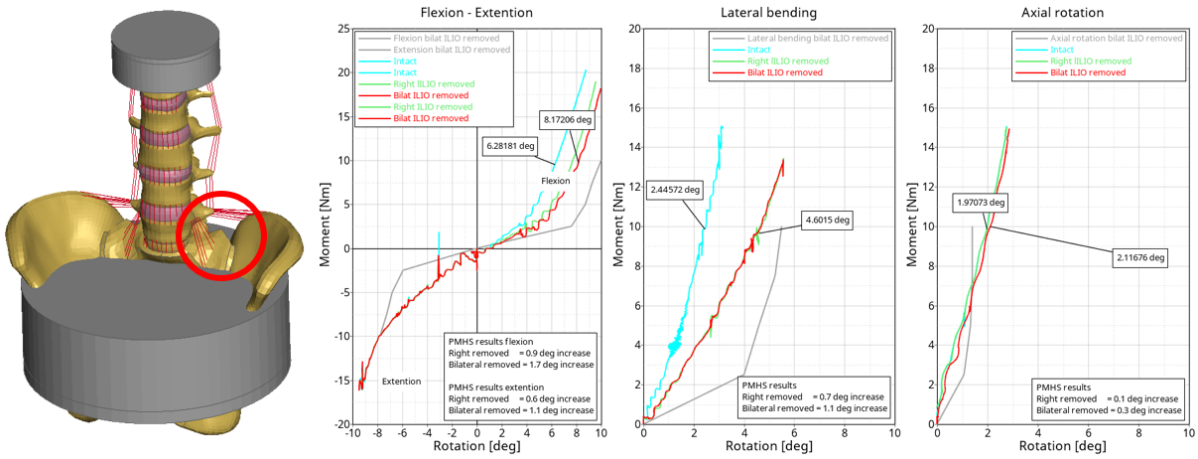

Figure 36. The effect of removing the iliolumbar ligaments. The blue curves represent model prediction of an intact model. The green curve, when the right ILIO ligaments are removed, and the red when ILIO ligaments are removed on both sides.

The tissue based IRF was compared to two other (force based) IRFs (Stemper et al., 2018; Tushak et al., 2023) and to combined flexion and compression tests performed by (Ortiz-Paparoni et al., 2021), see Figure 37. Generally, the predictions of the tissue based IRF are slightly conservative (lower force for same risk) compared to the Ortiz-Paparoni et al. results (black lines). The main reason for this is most likely that the tissue based IRF predicts onset of (endplate) fracture, while the Ortiz-Paparoni et al. results are for complete vertebrae fracture.

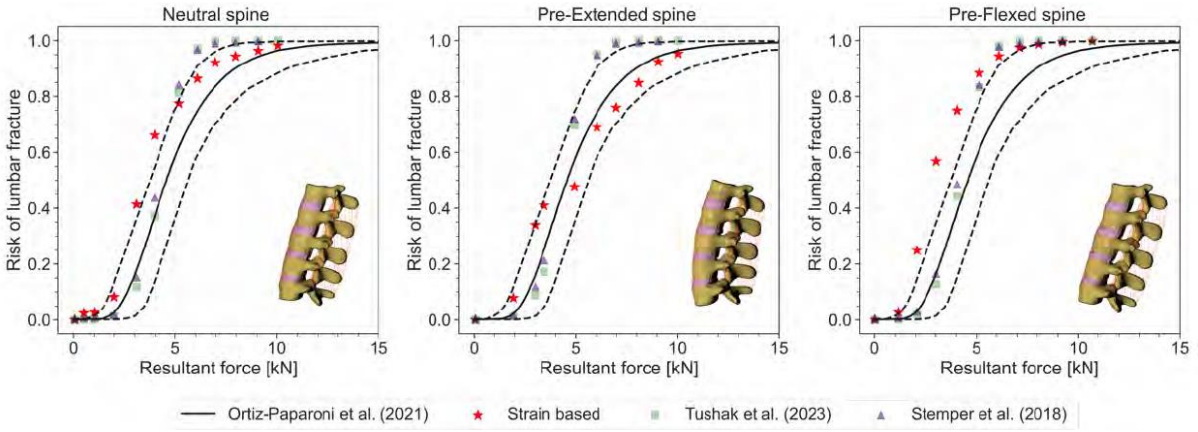

Figure 37. The predictions by the IRF (red stars) compared to force based IRFs by Tushak et al (green squares) and Stemper et al (purple triangles), to data from Ortiz-Paparoni et al using three levels of spine curvatures. From (Iraeus et al., 2023).

3.4. Cervical and Thoracic Spine Validation

The cervical spine kinetics and kinematics were compared to (Yoganandan et al., 1996) in tension, (Nightingale et al., 2002) in flexion and extension, and (Panjabi et al., 2001) in axial rotation and lateral bending. The thoracic spine kinetics and kinematics were validated to (Wilke et al., 2017) in flexion, extension, axial rotation and lateral bending, and to (Panjabi et al., 1976) for compression and tension. Except for the Yoganandan et al. tension test, validation is available in the validation repository for SAFER HBM v11.

In Figure 38 the model response is compared to biological tests (isolated cervical spine and full neck) presented by (Yoganandan et al., 1996). The predicted, isolated spine response for SAFER HBM is on the stiffer and stronger side closer to the full neck response.

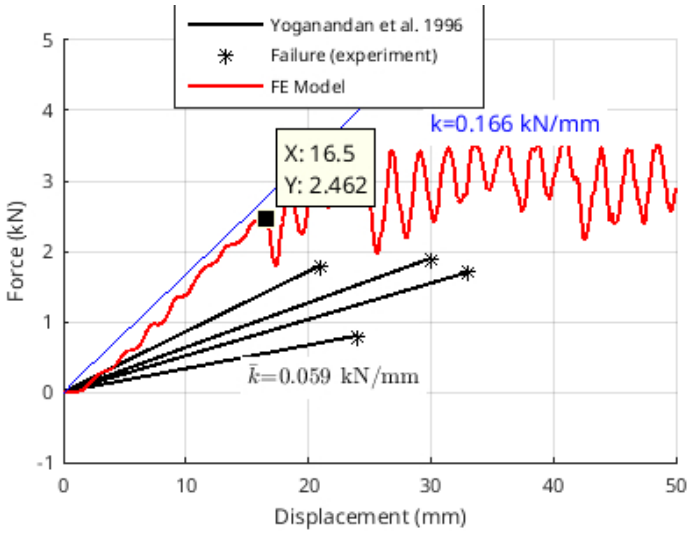

Figure 38. The cervical spine model compared to spine tension tests by (Yoganandan et al., 1996). The red line corresponds to the model prediction. The black lines represent four tests 0.059 kN/mm is the average stiffness in those tests, and the blue line and 0.166 kN/mm is the stiffness for tests with a full neck.

3.5. Clavicula and Humerus Validation

The kinematics and kinetics of the clavicula were validated to 3-p bending and axial loading test performed by (Zhang et al., 2014). The humerus was validated to 3-p bending tests performed by (Kemper et al., 2005). Finally, the upper arm, including soft tissue, was validated to 3-p bending tests performed by (Duma et al., 1999), and compression tests performed by (Kemper et al., 2005; Kemper, 2013). This validation is available in the validation repository for SAFER HBM v11.

3.6. Costovertebral joint Tuning

As no material data was available for the ligaments of the costovertebral joint, the material properties were tuned to get a reasonable kinematic and kinetic response of the overall joint. For this, parameter optimization was carried out using LS-OPT. The optimization objective was to minimize the difference between the model prediction and the test response (moment vs rotation) presented by (Duprey et al., 2010),

simultaneously for five loading directions. The result of this optimization for rib level 6 can be seen in Figure 39.

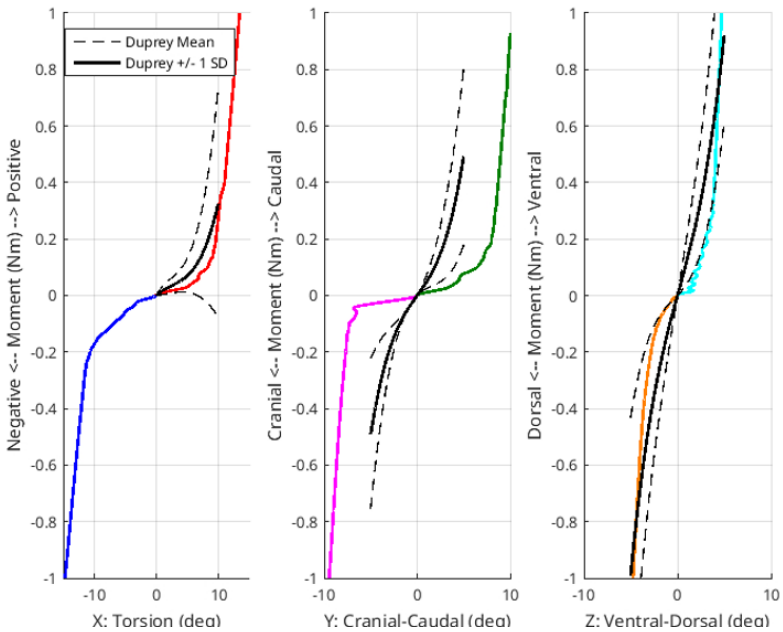

Figure 39. The stiffness of the modelled costovertebral joint (at rib 6) in torsion, cranial-caudal bending and ventral-dorsal bending (in different colors), compared to (Duprey et al., 2010) (showed with black lines).

To check the generaliziability of the tuned material parameters, rib 2 was modelled with the same strategy. It turned out that this joint matched the reference data even better than the prototype level, see Figure 40. This indicates that the modelling strategy has potential to be biofidelic for more levels, but more work is needed to verify this.

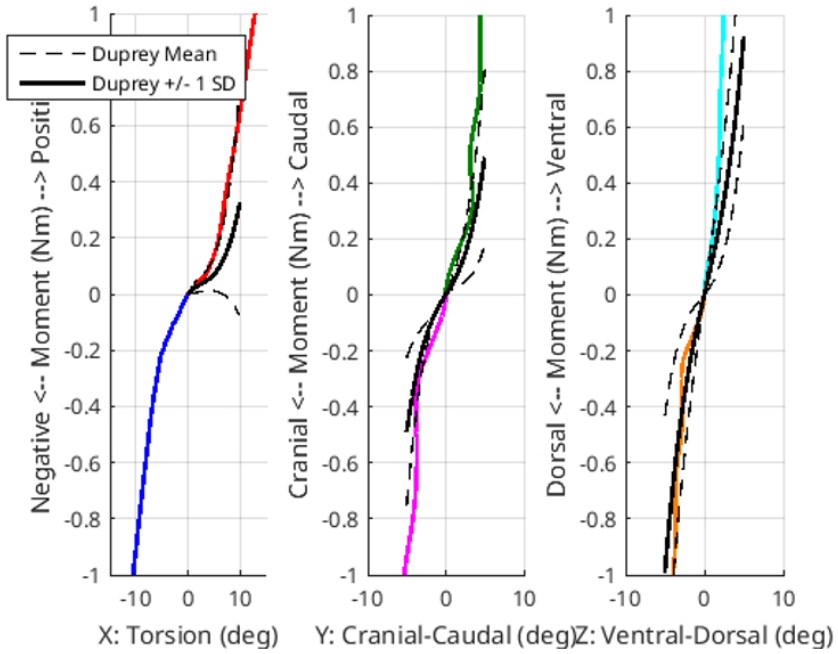

Figure 40. The stiffness of the modelled costovertebral joint (at rib 2) in torsion, cranial-caudal bending and ventral-dorsal bending (in different colors), compared to (Duprey et al., 2010) (showed with black lines).

3.7. Soft Tissue Validation

The pelvis and soft tissue updates were validated by gravity settling simulations, free-back rigid bar abdominal impacts (Hardy et al., 2001), stationary belt pull tests (Uriot et al., 2006), whole body lumbar flexion (Uriot, Potier, Baudrit, Trosseille, Richard, et al., 2015), sled test with rigid seat (Luet et al., 2012), sled test with semi-rigid seat (Uriot, Potier, Baudrit, Trosseille, Petit, et al., 2015) and sled test with reclined occupant on a semi-rigid seat (Richardson et al., 2020). The results of these validations can be seen in (Brynskog et al., 2024a) and (Brynskog et al., 2024b).

3.8. Effect of Updated Muscle Elements

The cervical spine maximum strength was evaluated after the updated muscle routing. The T1 vertebra and shoulder girdle were constrained, and a 1 m long steel cable was attached to the center of gravity of the head of the model, at a 90° angle. The force recorded in the cable was multiplied with the lever arm of 213 mm for this attachment to give maximum flexion, extension and lateral bending moments comparable with volunteer studies in the literature (Jordan et al., 1999; O'Leary et al., 2017; Östh et al., 2013; Queisser et al., 1994; Vasavada et al., 2001). The cervical strength of the model after the routing update was marginally lower than before the routing update due to the reduced muscle lever arms with a routing closer to the cervical spine. The model cervical strength matched the available volunteer data, except for the model being stronger in lateral bending.

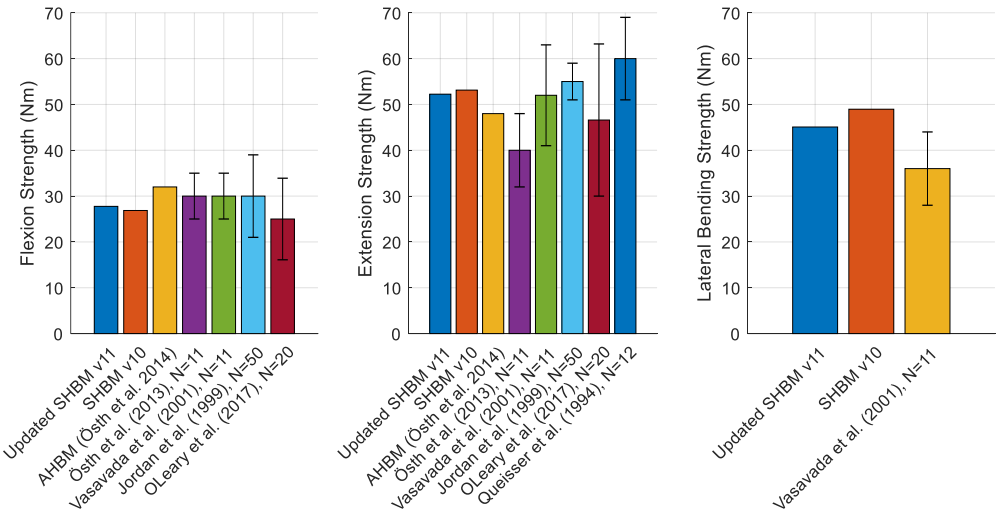

Figure 41. SAFER HBM v11 cervical spine strength after muscle routing update.

For evaluation of maximal lumbar flexion, extension and lateral bending moments, the pelvis and femora were constrained in space, and the 1 m long steel cable was attached to the T6 vertebra at approximate axilla height to match available volunteer tests (Ghezelbash et al., 2018; Larivière et al., 2009; McNeill et al., 1980; Ng et al., 2001; Östh et al., 2013) with a lever arm of 346 mm to the L5-sacrum joint. For the maximum strength simulations, the abdominal muscles (rectus abdominis and rectus obliques)

were activated to 100% for lumbar flexion, the paravertebral muscles (multifidus, erector spinae, quadratus lumborum etc.) for extension and a combination of muscles for lateral bending. It can be noted that the model is on the weak side compared with the volunteer data, Figure 42. For lumbar flexion, if maximal activation to the psoas muscle is also included the peak flexion strength increases to 108 Nm, which is in line with the reported volunteer strengths.

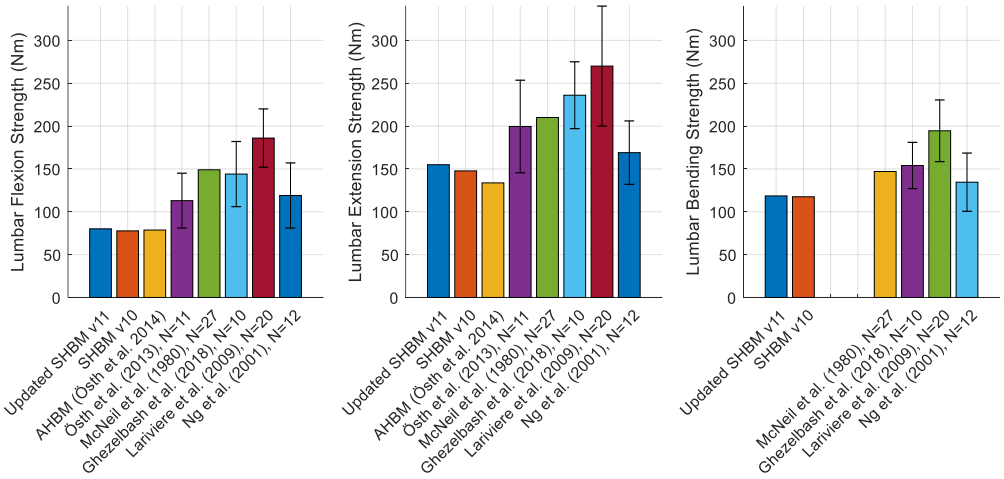

Figure 42. SAFER HBM v11 lumbar strength after muscle routing update. Flexion (left), Extension (middle), and Lateral bending (right).

4. Discussion

The overall aim of the SAFER HBM is to be an “omnidirectional, tunable and scalable human body model capable of injury risk and biofidelic kinematics prediction in high-g as well as low-g events”. A major part of the updates presented in this report, for SAFER HBM version 11, are related to injury prediction for reclined occupants in front crashes. This includes the updates to the pelvis, lumbar spine and the soft tissues in the hip area.

In addition, the model has been prepared for tissue-based injury prediction in other body parts, such as the femur, the shoulder girdle bones, and the thoracic and cervical spine. For the long bones, the cortical bone (outer layer) was modelled using solid elements. This was mainly done as the cortical thickness of these bones are larger than, e.g., the cortex of the ribs or the vertebrae (which are modelled using shell elements), and as a shell approximation is questionable for the cortex long bones, given the thickness to curvature ratio of those bones. However, parts of these bones, like the distal and proximal ends, also include a rather thin cortex. This means that one solid element over the cortical thickness, in these specific areas, results in mass scaling, even with a time step as small as 0.5 µs. Also, when only having one element over the thickness it is important to use fully integrated elements, to get at least two integration points over the thickness, and thus be able to capture some of the bending stiffness over the cortex local thickness axis.

The soft tissues were mainly updated to enhance submarining prediction and low-g events, but for the lower arm and the lower leg, also to improve mesh quality after the introduction of new long bone meshes in version 10 for these body parts. The element formulation used for the solids was mainly fully integrated 8-point hexahedron with an assumed strain approach to avoid shear locking seen in standard fully integrated elements, intended for elements with poor aspect ratios (ELFORM = -2 in LS-DYNA). While the elements in the HBM typically have an aspect ratio below 5 (in many cases close to one) in the lap belt area, the compression from belt loading in simulated crashes may increase the elements aspect ratio and make them sensitive to shear locking at the time of submarining, which then could prevent the submarining to some extent.

It can also be noted that a proper muscle material model is missing, and that a stiff form of fat tissue (Naseri, 2022) instead had to be implemented for SAFER HBM version 11. During the project another biofidelic muscle implementation (Lanzl et al., 2021) was tested. While being biofidelic, it turned out that it was not stable for large deformations (typically seen in submarining) and thus had to be rejected.

The muscle elements were re-routed to increase the biofidelity of the active HBM, where it has been hypothesized in earlier studies that the lumbar spine controller (with the active muscles) provides less moment than it should. The updated muscle routing provided some more strength, but the model is still on the weak side for the lumbar muscles and motions.

For several body parts the SAFER HBM geometry is based on statistical shape models (SSMs). These models predict the shape of various body parts, as function of independent variables like age, sex, stature and BMI. It is thus possible to create geometries representing the average of a subpopulation, like average males. Currently, the rib cage, the pelvis, and most of the outer shape are based on SSMs. During the work with version 11, several body parts were re-meshed, based on the geometry of an average sized female, and then scaled to fit the SAFER HBM. This includes the femur, the bones of the shoulder girdle, and the thoracic and cervical spine. Although basing the scaling (from female to male) on literature data, there is a risk that some female specific characteristics are still present in the (male) model. When SSMs become available for these body parts, it is recommended to check, and if necessary, adjust the geometries.

Finally, the model was renumbered, and the properties renamed, for easier model management. All model entities are now within a 5M range, enabling the possibility to have two SAFER HBMs within a 10M range. If more HBMs are to be included in a simulation for some specific test setup, it is mainly the nodes and elements that need to be within the 5M range. Most other entities are confined within a 1M range.

With the latest updates to SAFER HBM, the model is now stand-alone, free from proprietary data, and can be used for prediction of submarining for reclined occupants in front crashes.

5. References

Aira, J., Guleyupoglu, B., Jones, D., Koya, B., Davis, M., & Gayzik, F. S. (2019). Validated thoracic vertebrae and costovertebral joints increase biofidelity of a human body model in hub impacts. *Traffic Injury Prevention*, *20*(sup2), S1-S6.

Alicioglu, B., Kartal, O., Gurbuz, H., & Sut, N. (2008). Symphysis pubis distance in adults: a retrospective computed tomography study. *Surgical and radiologic anatomy*, *30*, 153-157.

Alonso, F., & Hart, D. (2014). Intervertebral disk. In *Encyclopedia of the Neurological Sciences* (Vol. 2, pp. 724-729). Elsevier.

Asano, S., Kaneda, K., Umehara, S., & Tadano, S. (1992). The Mechanical Properties of the Human L4–5 Functional Spinal Unit During Cyclic Loading: The Structural Effects of the Posterior Elements. *Spine*, *17*(11), 1343-1352. https://journals.lww.com/spinejournal/Fulltext/1992/11000/The_Mechanical_Properties_of_the_Human_L4_5.14.aspx

Bayat, M., & Pongpairote, N. (2020). *Arm Injury Prediction with THUMS SAFER - Improvements of the THUMS SAFER upper extremity* KTH ROYAL INSTITUTE OF TECHNOLOGY SCHOOL OF ENGINEERING SCIENCES]. STOCKHOLM, SWEDEN.

Bayraktar, H. H., Morgan, E. F., Niebur, G. L., Morris, G. E., Wong, E. K., & Keaveny, T. M. (2004). Comparison of the elastic and yield properties of human femoral trabecular and cortical bone tissue. *Journal of biomechanics*, *37*(1), 27-35.

Brinckmann, P., Biggemann, M., & Hilweg, D. (1989). Prediction of the compressive strength of human lumbar vertebrae. *Clinical Biomechanics*, *4*, iii-27.

Brynskog, E., Iraeus, J., Pipkorn, B., & Davidsson, J. (2022). Population Variance in Pelvic Response to Lateral Impacts–A Global Sensitivity Analysis.

Brynskog, E., Iraeus, J., Pipkorn, B., & Davidsson, J. (2024a). SAFER HBM model development for enhanced submarining prediction. *Chalmers University of Technology, REPORT*, *2024*, 03.

Brynskog, E., Iraeus, J., Pipkorn, B., & Davidsson, J. (2024b). Simulating Pelvis Kinematics from Belt and Seat Loading in Frontal Car Crash Scenarios: Important Boundary Conditions that Influence the Outcome. *Annals of Biomedical Engineering*, 1-30.

Brynskog, E., Iraeus, J., Reed, M. P., & Davidsson, J. (2021). Predicting pelvis geometry using a morphometric model with overall anthropometric variables. *Journal of biomechanics*, *126*, 110633.

Busscher, I., Ploegmakers, J. J., Verkerke, G. J., & Veldhuizen, A. G. (2010). Comparative anatomical dimensions of the complete human and porcine spine. *European Spine Journal*, *19*(7), 1104-1114.

Casaroli, G., Bassani, T., Brayda-Bruno, M., Luca, A., & Galbusera, F. (2020). What do we know about the biomechanics of the sacroiliac joint and of sacropelvic fixation? A literature review. *Medical engineering & physics*, *76*, 1-12.

Cassidy, J., Hiltner, A., & Baer, E. (1989). Hierarchical structure of the intervertebral disc. *Connective tissue research*, *23*(1), 75-88.

Chazal, J., Tanguy, A., Bourges, M., Gaurel, G., Escande, G., Guillot, M., & Vanneuville, G. (1985). Biomechanical properties of spinal ligaments and a histological study of the supraspinal ligament in traction. *Journal of biomechanics*, *18*(3), 167-176.

Dakin, G. J., Arbelaez, R. A., Molz IV, F. J., Alonso, J. E., Mann, K. A., & Eberhardt, A. W. (2001). Elastic and viscoelastic properties of the human pubic symphysis joint: effects of lateral impact loading. *J. Biomech. Eng.*, *123*(3), 218-226.

Dalstra, M., & Huiskes, R. (1995). Load transfer across the pelvic bone. *Journal of biomechanics*, *28*(6), 715-724.

Demetropoulos, C. K., Yang, K. H., Grimm, M. J., Khalil, T. B., & King, A. I. (1998). Mechanical properties of the cadaveric and Hybrid III lumbar spines. *SAE transactions*, 2862-2871.

Drew, A. J., Tashjian, R. Z., Henninger, H. B., & Bachus, K. N. (2019). Sex and laterality differences in medullary humerus morphology. *The Anatomical Record*, *302*(10), 1709-1717.

Du, W., Zhang, J., & Hu, J. (2018). A method to determine cortical bone thickness of human femur and tibia using clinical CT scans. 2018 IRCOBI conference proceedings, Athens (Greece),

Duma, S. M., Kemper, A. R., McNeely, D. M., Brolinson, P. G., & Matsuoka, F. (2006). Biomechanical response of the lumbar spine in dynamic compression. *Biomedical sciences instrumentation*, *42*, 476-481.

Duma, S. M., SCHREIBER, P. H., McMASTER, J. D., CRANDALL, J. R., Bass, C. R., & Pilkey, W. D. (1999). Dynamic injury tolerances for long bones of the female upper extremity. *The Journal of Anatomy*, *194*(3), 463-471.

Dunham, C. E., Takaki, S. E., Johnson, J. A., & Dunning, C. E. (2005). Mechanical properties of cancellous bone of the distal humerus. *Clinical Biomechanics*, *20*(8), 834-838.

Duprey, S., Subit, D., Guillemot, H., & Kent, R. W. (2010). Biomechanical properties of the costovertebral joint. *Medical engineering & physics*, *32*(2), 222-227.

Edwards, W. T., Zheng, Y., Ferrara, L. A., & Yuan, H. A. (2001). Structural features and thickness of the vertebral cortex in the thoracolumbar spine. *Spine*, *26*(2), 218-225.

Fahlstedt, M., Meng, S., & Kleiven, S. (2022). Influence of Strain Post-Processing on Brain Injury Prediction. *Journal of biomechanics*, 110940.

Gayzik, F., Moreno, D., Geer, C., Wuertzer, S., Martin, R., & Stitzel, J. (2011). Development of a full body CAD dataset for computational modeling: a multi-modality approach. *Annals of Biomedical Engineering*, *39*(10), 2568-2583.

Ghezelbash, F., El Ouaaid, Z., Shirazi-Adl, A., Plamondon, A., & Arjmand, N. (2018). Trunk musculoskeletal response in maximum voluntary exertions: A combined measurement-modeling investigation. *Journal of biomechanics*, *70*, 124-133.

Granhed, H., Jonson, R., & Hansson, T. (1989). Mineral content and strength of lumbar vertebrae A cadaver study. *Acta Orthopaedica Scandinavica*, *60*(1), 105-109.

Guillemot, H., Got, C., Besnault, B., Lavaste, F., Robin, S., Le Coz, J. Y., & Lassau, J.-P. (1998). Pelvic behavior in side collisions: static and dynamic tests on isolated pelvic bones. Proceedings of the 16th International Technical Conference of the Enhanced Safety of Vehicles,

Hammer, N., Steinke, H., Slowik, V., Josten, C., Stadler, J., Böhme, J., & Spanel-Borowski, K. (2009). The sacrotuberous and the sacrospinous ligament–a virtual reconstruction. *Annals of Anatomy-Anatomischer Anzeiger*, *191*(4), 417-425.

Hardy, W. N., Schneider, L. W., & Rouhana, S. W. (2001). *Abdominal impact response to rigid-bar, seatbelt, and airbag loading*.

Harris, M. D., Anderson, A. E., Henak, C. R., Ellis, B. J., Peters, C. L., & Weiss, J. A. (2012). Finite element prediction of cartilage contact stresses in normal human hips. *Journal of orthopaedic research*, *30*(7), 1133-1139.

Hedenstierna, S. (2008). *3D finite element modeling of cervical musculature and its effect on neck injury prevention* KTH].

Heuer, F., Schmidt, H., Klezl, Z., Claes, L., & Wilke, H.-J. (2007). Stepwise reduction of functional spinal structures increase range of motion and change lordosis angle. *Journal of biomechanics*, *40*(2), 271-280.

Holcombe, S. A., & Wang, S. C. (2014). Subcutaneous fat distribution in the human torso. *International Research Council on Biomechanics of Injury (IRC-14-43)*.

Holzapfel, G. A., Schulze-Bauer, C., Feigl, G., & Regitnig, P. (2005). Single lamellar mechanics of the human lumbar anulus fibrosus. *Biomechanics and modeling in mechanobiology*, *3*(3), 125-140.

Hutton, W., & Adams, M. (1982). Can the lumbar spine be crushed in heavy lifting? *Spine*, *7*(6), 586-590.

Iraeus, J., Brolin, K., & Pipkorn, B. (2020). Generic finite element models of human ribs, developed and validated for stiffness and strain prediction–To be used in rib fracture risk evaluation for the human population in vehicle crashes. *Journal of the mechanical behavior of biomedical materials*, 103742.

Iraeus, J., & Pipkorn, B. (2019, Sept 11-13). Development and Validation of a Generic Finite Element Ribcage to be used for Strain-based Fracture Prediction. 2019 International IRCOBI Conference,, Athens, Greece.

Iraeus, J., Poojary, Y. N., Jaber, L., John, J., & Davidsson, J. (2023). A new open-source finite element lumbar spine model, its tuning and validation, and development of a tissue-based injury risk function for compression fractures. *Nucleus*, *3*, 4.

ISO/TR 12350:2013. (2013). *Road vehicles -- Injury risk curves for the evaluation of occupant protection in side impact tests* (ISO/TR 12353-3:2013(E)).

Ivanov, A. A., Kiapour, A., Ebraheim, N. A., & Goel, V. (2009). Lumbar fusion leads to increases in angular motion and stress across sacroiliac joint: a finite element study. *Spine*, *34*(5), E162-E169.

Ivarsson, B. J., Genovese, D., Crandall, J. R., Bolton, J. R., Untaroiu, C. D., & Bose, D. (2009). The tolerance of the femoral shaft in combined axial compression and bending loading. *Stapp car crash journal*, *53*, 251-290. http://www.scopus.com/inward/record.url?eid=2-s2.0-75749137387&partnerID=40&md5=5b63c4ccdf37466e6b69d72b216bdd45

Izumiyama, T., Nishida, N., Iwanaga, H., Chen, X., Ohgi, J., Mori, K., Hayashi, T., Sakuramoto, I., Asahi, R., & Sugimoto, S. (2018). The analysis of an individual difference in human skeletal alignment in seated posture and occupant behavior using HBMs. Proceedings of the International Research Conference on the Biomechanics of Impact, IRCOBI, Athens, Greece, 12th September-14th September. IRC-18-84,

Jamison, D., Cannella, M., Pierce, E. C., & Marcolongo, M. S. (2013). A comparison of the human lumbar intervertebral disc mechanical response to normal and impact loading conditions. *Journal of biomechanical engineering*, *135*(9).

Jaramillo, H. E., Puttlitz, C. M., McGilvray, K., & García, J. J. (2016). Characterization of the L4–L5–S1 motion segment using the stepwise reduction method. *Journal of biomechanics*, *49*(7), 1248-1254.

Jordan, A., Mehlsen, J., Bülow, P. M., Østergaard, K., & Danneskiold-Samsøe, B. (1999). Maximal isometric strength of the cervical musculature in 100 healthy volunteers. *Spine*, *24*(13), 1343.

Kemper, A., Stitzel, J., Duma, S., Matsuoka, F., & Masuda, M. (2005). Biofidelity of the SID-IIs and a modified SID-IIs upper extremity: biomechanical properties of the human humerus. Proc. of the 19th Int. Tec. Conf. on the Enhanced Safety of Vehicles,

Kemper, A. R. (2013). Response corridors for the medial–lateral compressive stiffness of the human arm: Implications for side impact protection. *Accident Analysis & Prevention*, *50*, 204-222.

Kemper, A. R., McNally, C., & Duma, S. M. (2008). Dynamic tensile material properties of human pelvic cortical bone. *Biomedical sciences instrumentation*, *44*, 417-418.

Khor, F., Cronin, D. S., Watson, B., Gierczycka, D., & Malcolm, S. (2018). Importance of asymmetry and anisotropy in predicting cortical bone response and fracture using human body model femur in three-point bending and axial rotation. *Journal of the mechanical behavior of biomedical materials*, *87*, 213-229.

Klein, K. F., Hu, J., Reed, M. P., Hoff, C. N., & Rupp, J. D. (2015). Development and validation of statistical models of femur geometry for use with parametric finite element models. *Annals of Biomedical Engineering*, *43*(10), 2503-2514.

Kleiven, S. (2006). Evaluation of head injury criteria using a finite element model validated against experiments on localized brain motion, intracerebral acceleration, and intracranial pressure. *International Journal of Crashworthiness*, *11*(1), 65-79. http://www.scopus.com/inward/record.url?eid=2-s2.0-33646260214&partnerID=40&md5=4b6ca40bf9d277dc36dc821c404e228c

Kleiven, S. (2007). Predictors for traumatic brain injuries evaluated through accident reconstructions. *Stapp car crash journal*, *51*, 81-114. http://www.scopus.com/inward/record.url?eid=2-s2.0-40649120734&partnerID=40&md5=0b7958ea23f5133f4b7221ec056c23c0

Kleiven, S., & Hardy, W. (2002). Correlation of an FE model of the Human Head with Experiments on localized Motion of the Brain—Consequences for Injury Prediction. 46th Stapp Car Crash Journal.

Kleiven, S., & Von Holst, H. (2002a). Consequences of head size following trauma to the human head. *Journal of biomechanics*, *35*(2), 153-160.

Kleiven, S., & Von Holst, H. (2002b). Consequences of reduced brain volume following impact in prediction of subdural hematoma evaluated with numerical techniques. *Traffic Injury Prevention*, *3*(4), 303-310.

Kopperdahl, D. L., & Keaveny, T. M. (1998). Yield strain behavior of trabecular bone. *Journal of biomechanics*, *31*(7), 601-608.

Kopperdahl, D. L., Morgan, E. F., & Keaveny, T. M. (2002). Quantitative computed tomography estimates of the mechanical properties of human vertebral trabecular bone. *Journal of orthopaedic research*, *20*(4), 801-805.

Lanzl, F., Berger, A., Huehn, D., Dussinger, S., Ghosh, P., Mayer, C., Martynenko, O., Naseri, H., Iraeus, J., & Peldschus, S. (2021). Simplified multi-code model for passive muscle tissue under impact. *International Research Council on Biomechanics of Injury IRCOBI.[Google Scholar]*.

Larivière, C., Gagnon, D., & Genest, K. (2009). Offering proper feedback to control for out-of-plane lumbar moments influences the activity of trunk muscles during unidirectional isometric trunk exertions. *Journal of biomechanics*, *42*(10), 1498-1505.

Larsson, E. (2020). *SAFER HBM in 9kph sled simulations* (2020:04).

Larsson, E., Iraeus, J., & Davidsson, J. (2023). Investigating sources for variability in volunteer kinematics in a braking maneuver, a sensitivity analysis with an active human body model. *Frontiers in bioengineering and biotechnology*, *11*, 1203959.

Larsson, E., Iraeus, J., Fice, J., Pipkorn, B., Jakobsson, L., Brynskog, E., Brolin, K., & Davidsson, J. (2019). Active human body model predictions compared to volunteer response in experiments with braking, lane change, and combined manoeuvres. the International IRCOBI Conference, Florence, Italy.

Larsson, K.-J., Blennow, A., Iraeus, J., Pipkorn, B., & Lubbe, N. (2021). Rib cortical bone fracture risk as a function of age and rib strain: updated injury prediction using finite element human body models. *Frontiers in bioengineering and biotechnology*, *9*, 412.

Lian, L., Baek, M., Jones, S. M. M., & Hu, J. (2023). A Parametric Thoracic Spine Model Accounting for Geometric Variations by Age, Sex, Stature, and Body Mass Index.

Lu, Y.-C., & Untaroiu, C. D. (2013). Statistical shape analysis of clavicular cortical bone with applications to the development of mean and boundary shape models. *Computer methods and programs in biomedicine*, *111*(3), 613-628.

Luet, C., Trosseille, X., Drazétic, P., Potier, P., & Vallancien, G. (2012). *Kinematics and Dynamics of the Pelvis in the Process of Submarining using PMHS Sled Tests*.

Malo, M., Rohrbach, D., Isaksson, H., Töyräs, J., Jurvelin, J., Tamminen, I., Kröger, H., & Raum, K. (2013). Longitudinal elastic properties and porosity of cortical bone tissue vary with age in human proximal femur. *Bone*, *53*(2), 451-458.

Marini, G., Studer, H., Huber, G., Püschel, K., & Ferguson, S. J. (2016). Geometrical aspects of patient-specific modelling of the intervertebral disc: Collagen fibre orientation and residual stress distribution. *Biomechanics and modeling in mechanobiology*, *15*(3), 543-560.

Markolf, K. L., & Morris, J. M. (1974). The structural components of the intervertebral disc: a study of their contributions to the ability of the disc to withstand compressive forces. *JBJS*, *56*(4), 675-687.

Martin, R. B., Burr, D. B., Sharkey, N. A., & Fyhrie, D. P. (1998). *Skeletal tissue mechanics* (Vol. 190). Springer.

Mattucci, S. F., & Cronin, D. S. (2015). A method to characterize average cervical spine ligament response based on raw data sets for implementation into injury biomechanics models. *Journal of the mechanical behavior of biomedical materials*, *41*, 251-260.

Mattucci, S. F., Moulton, J. A., Chandrashekar, N., & Cronin, D. S. (2013). Strain rate dependent properties of human craniovertebral ligaments. *Journal of the mechanical behavior of biomedical materials*, *23*, 71-79.

McNeill, T., Warwick, D., Andersson, G., & Schultz, A. (1980). Trunk strengths in attempted flexion, extension, and lateral bending in healthy subjects and patients with low-back disorders. *Spine*, *5*(6), 529-538.

Mendoza-Vazquez, M., Brolin, K., Davidsson, J., & Wismans, J. (2013). Human rib response to different restraint systems in frontal impacts: a study using a human body model. *International Journal of Crashworthiness*, *18*(5), 516-529.

Miller, J. A., Schultz, A. B., & Andersson, G. B. (1987). Load-displacement behavior of sacroiliac joints. *Journal of orthopaedic research*, *5*(1), 92-101.

Nahum, A. M., & Melvin, J. W. (2012). *Accidental injury: biomechanics and prevention*. Springer Science & Business Media.

Naseri, H. (2022). *Calibration of Adipose tissue material properties in LS-DYNA* (Research report - Department of Mechanics and Maritime Sciences, Issue.

Newell, N., Little, J., Christou, A., Adams, M., Adam, C., & Masouros, S. (2017). Biomechanics of the human intervertebral disc: A review of testing techniques and results. *Journal of the mechanical behavior of biomedical materials*, *69*, 420-434.

Ng, J. K. F., Parnianpour, M., Richardson, C. A., & Kippers, V. (2001). Functional roles of abdominal and back muscles during isometric axial rotation of the trunk. *Journal of orthopaedic research*, *19*(3), 463-471.

Nightingale, R. W., Winkelstein, B. A., Knaub, K. E., Richardson, W. J., Luck, J. F., & Myers, B. S. (2002). Comparative strengths and structural properties of the upper and lower cervical spine in flexion and extension. *Journal of biomechanics*, *35*(6), 725-732.

Nishida, N., Izumiyama, T., Asahi, R., Iwanaga, H., Yamagata, H., Mihara, A., Nakashima, D., Imajo, Y., Suzuki, H., & Funaba, M. (2020). Changes in the global spine alignment in the sitting position in an automobile. *The Spine Journal*, *20*(4), 614-620.

Nolte, L. P., Panjabi, M., & Oxland, T. (1990). Biomechanical properties of lumbar spinal ligaments. *Clinical implant materials, advances in biomaterials*, *9*, 663-668.

O'Leary, S., Fagermoen, C. L., Hasegawa, H., Thorsen, A.-S. S., & Van Wyk, L. (2017). Differential strength and endurance parameters of the craniocervical and cervicothoracic extensors and flexors in healthy individuals. *Journal of applied biomechanics*, *33*(2), 166-170.

Ólafsdóttir, J., Östh, J., & Brolin, K. (2019). Modelling Reflex Recruitment of Neck Muscles in a Finite Element Human Body Model for Simulating Omnidirectional Head Kinematics. the International IRCOBI Conference, Florence, Italy.

Ortiz-Paparoni, M., Op't Eynde, J., Kait, J., Bigler, B., Shridharani, J., Schmidt, A., Cox, C., Morino, C., Pintar, F., & Yoganandan, N. (2021). The human lumbar spine during high-rate under seat loading: a combined metric injury criteria. *Annals of Biomedical Engineering*, *49*, 3018-3030.

Östh, J., Brolin, K., & Bråse, D. (2015). A human body model with active muscles for simulation of pretensioned restraints in autonomous braking interventions. *Traffic Injury Prevention*, *16*(3), 304-313.

Östh, J., Brolin, K., Carlsson, S., Wismans, J., & Davidsson, J. (2012). The occupant response to autonomous braking: a modeling approach that accounts for active musculature. *Traffic Injury Prevention*, *13*(3), 265-277.

Östh, J., Brolin, K., Svensson, M. Y., & Linder, A. (2016). A female ligamentous cervical spine finite element model validated for physiological loads. *Journal of biomechanical engineering*, *138*(6).

Östh, J., Ólafsdóttir, J. M., Davidsson, J., & Brolin, K. (2013). Driver kinematic and muscle responses in braking events with standard and reversible pre-tensioned restraints: validation data for human models. *Stapp car crash journal*, *57*, 1.

Panjabi, M. M., Brand Jr, R., & White 3rd, A. (1976). Mechanical properties of the human thoracic spine as shown by three-dimensional load-displacement curves. *JBJS*, *58*(5), 642-652.

Panjabi, M. M., Chen, N. C., Shin, E. K., & Wang, J.-L. (2001). The cortical shell architecture of human cervical vertebral bodies. *Spine*, *26*(22), 2478-2484.

Panjabi, M. M., Oxland, T. R., & Parks, E. H. (1991). Quantitative anatomy of cervical spine ligaments. Part I. Upper cervical spine. *Clinical Spine Surgery*, *4*(3), 270-276.

Panjabi, M. M., Takata, K., Goel, V., Federico, D., Oxland, T., Duranceau, J., & Krag, M. (1991). Thoracic human vertebrae. Quantitative three-dimensional anatomy. *Spine*, *16*(8), 888-901.

Panzer, M. B., & Cronin, D. S. (2009). C4–C5 segment finite element model development, validation, and load-sharing investigation. *Journal of biomechanics*, *42*(4), 480-490.

Park, B.-K. D., Jones, M. L., Ebert, S., & Reed, M. P. (2022). A parametric modeling of adult body shape in a supported seated posture including effects of age. *Ergonomics*, *65*(6), 795-803.

Peretz, A. M., Hipp, J. A., & Heggeness, M. H. (1998). The internal bony architecture of the sacrum. *Spine*, *23*(9), 971-974.

Pipkorn, B., Iraeus, J., Bjorklund, M., Bunketorp, O., & Jakobsson, L. (2019). Multi-Scale validation of a rib fracture prediction method for human body models. the International IRCOBI Conference, Online.

Pipkorn, B., Jakobsson, L., Iraeus, J., & Östh, J. (2023). THE SAFER HBM–A human body model for seamless integrated occupant analysis for all road users. 27th International Technical Conference on the Enhanced Safety of Vehicles (ESV) National Highway Traffic Safety Administration,

Pipkorn, B., Östh, J., Brynskog, E., Larsson, E., Rydqvist, L., Iraeus, J., Perez-Rapela, D., & Jakobsson, L. (2021). Validation of the SAFER Human Body Model Kinematics in Far-Side Impacts. the International IRCOBI Conference, Online.

Queisser, F., Blüthner, R., & Seidel, H. (1994). Control of positioning the cervical spine and its application to measuring extensor strength. *Clinical Biomechanics*, *9*(3), 157-161.

Rater, J.-F. (2013). *Thorax soft tissue response for validation of human body models and injury prediction* Master's Thesis 2013: 07. Chalmers University of Technology, Gothenburg, Sweden].

Reed, M. P., & Ebert, S. M. (2013). *Elderly occupants: posture, body shape, and belt fit*.

Reilly, D. T., & Burstein, A. H. (1975). The elastic and ultimate properties of compact bone tissue. *Journal of biomechanics*, *8*(6), 393-405.

Richards, A. M., Coleman, N. W., Knight, T. A., Belkoff, S. M., & Mears, S. C. (2010). Bone density and cortical thickness in normal, osteopenic, and osteoporotic sacra. *Journal of osteoporosis*, *2010*(1), 504078.

Richardson, R., Donlon, J.-P., Jayathirtha, M., Forman, J. L., Shaw, G., Östling, M., Mroz, K., & Pipkorn, B. (2020). Kinematic and injury response of reclined PMHS in frontal impacts. *Stapp car crash journal*, *64*, 83-153.

Ritzel, H., Amling, M., Pösl, M., Hahn, M., & Delling, G. (1997). The thickness of human vertebral cortical bone and its changes in aging and osteoporosis: A histomorphometric analysis of the complete spinal column from thirty-seven autopsy specimens. *Journal of Bone and Mineral Research*, *12*(1), 89-95.

Roberts, C. (2020). *Sex-based Geometric Differences in the Lower Extremity and their Effect on Injury in the Automotive Crash Environment* [PhD,

Schneider, L. (1983). *Development of anthropometrically based design specifications for an advanced adult anthropomorphic dummy family, volume 1. final report*.

Scoles, P. V., Linton, A. E., Latimer, B., Levy, M. E., & Digiovanni, B. F. (1988). Vertebral body and posterior element morphology: the normal spine in middle life. *Spine*, *13*(10), 1082-1086.

Someya, K., Mochizuki, T., Hokari, S., Tanifuji, O., Katsumi, R., Koga, H., Takahashi, Y., Kobayashi, K., Morise, Y., & Sakamoto, M. (2020). Age-and sex-related characteristics in cortical thickness of femoral diaphysis for young and elderly subjects. *Journal of bone and mineral metabolism*, *38*, 533-543.

Stansfield, E., Mitteroecker, P., Umek, W., & Fischer, B. (2023). The variation in shape and thickness of the pelvic floor musculature in males and females: a geometric-morphometric analysis. *International Urogynecology Journal*, *34*(2), 453-461.

Steinke, H., Hammer, N., Slowik, V., Stadler, J., Josten, C., Böhme, J., & Spanel-Borowski, K. (2010). Novel insights into the sacroiliac joint ligaments. *Spine*, *35*(3), 257-263.

Stemper, B. D., Chirvi, S., Doan, N., Baisden, J. L., Maiman, D. J., Curry, W. H., Yoganandan, N., Pintar, F. A., Paskoff, G., & Shender, B. S. (2018). Biomechanical tolerance of whole lumbar spines in straightened posture subjected to axial acceleration. *Journal of Orthopaedic Research®*, *36*(6), 1747-1756.

Svensson, G. (2022). Finite Element Modelling of Knee Joint and Femur for Future Injury Assessment.

Tahan, N., Khademi-Kalantari, K., Mohseni-Bandpei, M. A., Mikaili, S., Baghban, A. A., & Jaberzadeh, S. (2016). Measurement of superficial and deep abdominal muscle thickness: an ultrasonography study. *Journal of physiological anthropology*, *35*(1), 1-5.

Tushak, S. K., Donlon, J. P., Gepner, B. D., Chebbi, A., Pipkorn, B., Hallman, J. J., Forman, J. L., & Kerrigan, J. R. (2022). Failure tolerance of the human lumbar spine in dynamic combined compression and flexion loading. *Journal of biomechanics*, *135*, 111051.

Tushak, S. K., Gepner, B. D., Forman, J. L., Hallman, J. J., Pipkorn, B., & Kerrigan, J. R. (2023). Human lumbar spine injury risk in dynamic combined compression and flexion loading. *Annals of Biomedical Engineering*, 1-10.

Ulrich, D., Van Rietbergen, B., Laib, A., & Ruegsegger, P. (1999). The ability of three-dimensional structural indices to reflect mechanical aspects of trabecular bone. *Bone*, *25*(1), 55-60.

Uriot, J., Baudrit, P., Potier, P., Trosseille, X., Petit, P., Guillemot, H., Guérin, L., & Vallancien, G. (2006). Investigations on the belt-to-pelvis interaction in case of submarining. *Stapp car crash journal*, *50*, 53-73. http://www.scopus.com/inward/record.url?eid=2-s2.0-33947500534&partnerID=40&md5=b82c32de3a1b2a362319c67a65dbe0ac

Uriot, J., Potier, P., Baudrit, P., Trosseille, X., Petit, P., Richard, O., Compigne, S., Masuda, M., & Douard, R. (2015). Reference PMHS Sled Tests to Assess Submarining. *Stapp car crash journal*, *59*, 203-223.

Uriot, J., Potier, P., Baudrit, P., Trosseille, X., Richard, O., & Douard, R. (2015). Comparison of HII, HIII and THOR dummy responses with respect to PMHS sled tests. Proceedings of the International Research Conference on the Biomechanics of Impact, IRCOBI, Lyon, France, 9th September-11th September. IRC-15-55,

Vasavada, A. N., Li, S., & Delp, S. L. (2001). Three-dimensional isometric strength of neck muscles in humans. *Spine*, *26*(17), 1904-1909.

Wilke, H.-J., Herkommer, A., Werner, K., & Liebsch, C. (2017). In vitro analysis of the segmental flexibility of the thoracic spine. *PloS one*, *12*(5), e0177823.

Wu, Y., Loaiza, J., Banerji, R., Blouin, O., & Morgan, E. (2021). Structure-function relationships of the human vertebral endplate. *JOR Spine*, *4*(3), e1170.

Yamamoto, I., Panjabi, M., Oxland, T., & Crisco, J. (1990). The role of the iliolumbar ligament in the lumbosacral junction. *Spine*, *15*(11), 1138-1141.

Yamamoto, I., Panjabi, M. M., Crisco, T., & Oxland, T. (1989). Three-dimensional movements of the whole lumbar spine and lumbosacral joint. *Spine*, *14*(11), 1256-1260.

Yoganandan, N., Kumaresan, S., & Pintar, F. A. (2000). Geometric and mechanical properties of human cervical spine ligaments. *J. Biomech. Eng.*, *122*(6), 623-629.

Yoganandan, N., Pintar, F., Maiman, D., Cusick, J., Sances Jr, A., & Walsh, P. (1996). Human head-neck biomechanics under axial tension. *Medical engineering & physics*, *18*(4), 289-294.

Yoganandan, N., Pintar, F. A., Stemper, B. D., Baisden, J. L., Aktay, R., Shender, B. S., Paskoff, G., & Laud, P. (2006). Trabecular bone density of male human cervical and lumbar vertebrae. *Bone*, *39*(2), 336-344.

Zhai, X., Nauman, E. A., Nie, Y., Liao, H., Lycke, R. J., & Chen, W. W. (2019). Mechanical response of human muscle at intermediate strain rates. *Journal of biomechanical engineering*, *141*(4), 044506.

Zhang, Q., Kindig, M., Li, Z., Crandall, J. R., & Kerrigan, J. R. (2014). Development of structural and material clavicle response corridors under axial compression and three point bending loading for clavicle finite element model validation. *Journal of biomechanics*, *47*(11), 2563-2570.

Zhou, S., McCarthy, I., McGregor, A., Coombs, R., & Hughes, S. (2000). Geometrical dimensions of the lower lumbar vertebrae–analysis of data from digitised CT images. *European Spine Journal*, *9*, 242-248.

Appendix A – Element quality criteria

The element quality criteria that is used to model the SAFER HBM have previously been published in (Pipkorn et al., 2021), and are summaries here.

MESH QUALITY CRITERIA USED FOR UPDATES OF THE SAFER HBM (SOFTWARE WITHIN BRACKETS DEFINES CRITERIA). SUPER SCRIPTS REFERS TO PUBLICATIONS OR OTHER SOURCES USED AS BASIS FOR CRITERIA LEVELS. THE 100% LIMIT IS MAINLY FOR OVERALL MODEL STABILITY AND SHOULD THUS BE FULFILLED FOR THE WHOLE MODEL. AREAS OF HIGH IMPORTANCE, WHERE TISSUE-BASED INJURY CRITERIA SHOULD BE USED, SHOULD ALSO FULFILL THE 95% TARGET.

	Aspect Ratio [-]	Skewness [deg]	Warpage [deg]	Hexa Angle [deg]	Tetra Angle [deg]	Jacobian [-]
Solid Elements	(Patran)	(Patran)	(Patran)	(Abaqus)	(Abaqus)	(ANSA)
95 % Target	$<3^{a-c}$	$<45^{b}$	$<10^{c}$	$30<\phi<140^{c}$	$30<\phi<120^{b}$	$>0.7^{a,c}$
100 % Limit	$<10^{a,c}$	$<60^{b}$	$<20^{b}$	$20<\phi<160^{a}$	$20^{c}<\phi<150^{a}$	$>0.3^{c}$

	Aspect Ratio [-]	Skewness [deg]	Warpage [deg]	Quad Angle [deg]	Tria Angle [deg]	Jacobian [-]
Shell elements	(Patran)	(Patran)	(Patran)	(IDEAS)	(IDEAS)	(ANSA)
95 % Target	$<3^{a-c}$	$<30^{c}$	$<7^{c}$	$45<\phi<135^{b,c}$		$>0.7^{a,c}$
100 % Limit	$<10^{b}$	$<60^{b}$	$<20^{b}$	$20<\phi<160^{c}$	$30<\phi<120^{b,c}$	$>0.3^{c}$

[a] Burkhart, T. A., Andrews, D. M., & Dunning, C. E. (2013). Finite element modeling mesh quality, energy balance and validation methods: a review with recommendations associated with the modeling of bone tissue. *Journal of biomechanics, 46*(9), 1477-1488

[b] Yang, K.-H. (2017). *Basic finite element method as applied to injury biomechanics*: Academic Press.

[c] Industry requirements